# Cobalt ferrites CoxFe3-xO4 (x = 1 and x = 1.5) as photocatalysts under simulated sunlight: An experimental study coupled to predictive RSM approach

Yassine Elaadssi, Véronique Madigou, Madjid Arab

Journal Pre-proof


# Cobalt ferrites $Co_xFe_{3-x}O_4$ (x=1 and x=1.5) as photocatalysts under simulated sunlight: An experimental study coupled to predictive RSM approach

Yassine Elaadssi , Véronique Madigou , Madjid Arab

PII: S2468-0230(25)00912-5
DOI: https://doi.org/10.1016/j.surfin.2025.106655
Reference: SURFIN 106655

To appear in: *Surfaces and Interfaces*

Received date: 20 January 2025
Revised date: 9 April 2025
Accepted date: 7 May 2025

Please cite this article as: Yassine Elaadssi , Véronique Madigou , Madjid Arab , Cobalt ferrites $Co_xFe_{3-x}O_4$ (x=1 and x=1.5) as photocatalysts under simulated sunlight: An experimental study coupled to predictive RSM approach, *Surfaces and Interfaces* (2025), doi: https://doi.org/10.1016/j.surfin.2025.106655

# Cobalt ferrites $Co_xFe_{3-x}O_4$ (x = 1 and x = 1.5) as photocatalysts under simulated sunlight: An experimental study coupled to predictive RSM approach.

Yassine Elaadssi, Véronique Madigou, Madjid Arab.

Université de Toulon, Aix Marseille Univ, CNRS, IM2NP, CS 60584, CEDEX 9, F-83041 Toulon, France.

**Corresponding authors**: madjid.arab@univ-tln.fr.

## Abstract

This study explores the use of $Co_xFe_{3-x}O_4$ ferrites as photocatalyst for the degradation of a model pollutant (Rhodamine B). Two different compositions (x = 1 and 1.5) were synthesized by a hydrothermal route using nitrates as precursors. The structural studies showed that the powders consist of nanometric (8-9 nm) monocrystalline particles of octahedral shape. X-rays and electron diffraction results confirmed the cubic spinel structure. The n-type semiconductor behavior was confirmed using Mott Schottky method and the direct band gap energies were obtained from diffuse reflectance spectroscopy (DRS): 2.32 eV and 2.18 eV for $CoFe_2O_4$ and $Co_{1.5}Fe_{1.5}O_4$ respectively. Due to its lower charge transfer resistance (2.8 kΩ/cm$^2$), higher photocurrent density (1.18 µA/cm$^2$), and a longer lifetime (5.2 ns) of the photogenerated charges, the x = 1.5 composition presents the greatest potential for this application. The response surface methodology (RSM) based on Box-Behnken design (BBD) was used to optimize the rhodamine B photodegradation process under simulated sunlight: RhB concentration, pH and catalyst mass. Under optimal conditions, the dye was completely degraded in 180 minutes for x=1.5 while it was 240 minutes for x=1. Total organic carbon (TOC) analysis shows an advanced mineralization and achieves a higher removal rate of 96% for x=1.5 after 180 minutes. Hydroxyl radicals and photogenerated holes are detected as the dominant reactive species using radical scavenging experiments. An increase of cobalt concentration in ferrite-based catalysts improves photocatalytic efficiency by reducing bandgap energy and improving charge photogeneration and transfer processes.

**Keywords**: Response Surface Methodology. Cobalt ferrites. Dyes. Simulated sunlight irradiation. Photodegradation. Rhodamine B.

## 1. Introduction

Water pollution is a serious global problem that affects the environment and human health. As industries grow and cities expand, more untreated or poorly treated wastewater is being released into rivers, lakes, and oceans. This wastewater contains harmful substances like organic compounds, heavy metals, and germs, which can harm wildlife and people. To protect our water resources, it is crucial to improve wastewater treatment methods. [1–3].

Advanced Oxidation Processes (AOPs) offers a promising approach for wastewater treatment [4,5]. The reactions based on this process generate very reactive chemical species, such as for example hydroxyl and superoxide radical species ($OH^{\cdot}$ and $O^{2\bullet-}$) that can break down complex organic pollutant's molecules into smaller and less toxic species. Different materials have been explored for (AOPs), such as titanium dioxide ($TiO_2$) and zinc oxide (ZnO), which are known for their high bandgap energy and photocatalytic properties. [6,7]. More recently, another semiconductors compounds are considered, among them, ferrites are widely studied [8–10]. Cobalt ferrite nanoparticles are known for their many properties, optical, photoelectrochemical and chemical stability, making them highly suitable for photocatalytic applications. It is well known that small particles, which have a large specific area, improve photocatalytic activity. The morphology of the particles can also have a certain influence due to the fact that the crystallographic faces of the particles present a different cation distribution on the surfaces. The method of synthesis used to obtain $Co_xFe_{3-x}O_4$ nanoparticles is a key aspect of this study. The choice of a hydrothermal route is significant because it allows precise control of particle size, composition, crystallinity, and surface properties [11]. The morphology of the particles is more controlled by the use of surfactant. These parameters are decisive for the optimization of the photocatalyst's performance. In this study Rhodamine B (RhB), which is a synthetic dye used in the textile paper and leather industries, was chosen as a model pollutant. RhB is well known for its nondegradability, high chemical stability and solubility, which makes it a persistent pollutant, harmful to health and environment [12]. The photocatalytic degradation efficiency of RhB depends on several factors: the characteristics of the materials used (surface area, chemical composition, optical properties) [13,14] but also on the experimental conditions of the photocatalysis test. The optimization of these parameters can lead to the development of more effective photocatalysts.

This work presents a study on the synthesis and characterization of $Co_xFe_{3-x}O_4$ cobalt ferrite nanoparticles (x=1 and x=1.5) obtained from nitrates precursors. In literature, the studies focus on $AFe_2O_4$ type ferrites, such as $CoFe_2O_4$, with possible substitution of metallic cation A by another type of metallic cation leading to $M_xA_{1-x}Fe_2O_4$ formula. In this work, another composition $Co_{1.5}Fe_{1.5}O_4$,

for which iron cations are also substituted by cobalt cations, was synthesized and compared to the first one ($CoFe_2O_4$). The structural and physical properties of these materials were carried out to understand the degradation mechanism. This study is coupled with an optimization of some experimental parameters of the Rhodamine B degradation test thanks to the combination of Response Surface Methodology (RSM) and Box-Behnken Design (BBD) [15–18].We specifically focused on the optimization of the pH and RhB concentration of the polluted solution and catalyst amount. The influence of the composition on the structural, morphological, optical and photo-electrochemical properties of the nanoparticles was studied and its effect on the photocatalytic degradation efficiency was evaluated. The optimal conditions for the photocatalytic tests predicted by the RSM-BBD have been validated by experimental studies. The radicals trapping tests and TOC analyzes allow the identification of active chemical species but also the control of organic carbon. Finally, to explain the photocatalytic degradation potential mechanisms were proposed and discussed,

## 2. Materials and Methods

### 2.1. Chemicals and reactants

Cobalt (II) nitrate hexahydrate (Co $(NO_3)_2$-$6H_2O$) and iron (III) nitrate nanohydrate (Fe $(NO_3)_3$-$9H_2O$) have been used as cobalt and iron precursors, respectively. The sodium hydroxide (NaOH) was used to adjust the value of pH, while cetyltrimethylammonium bromide (CTAB, 98+%) was employed as surfactant to control the shape of the nanoparticles [19]. All chemicals' products were purchased from Sigma-Aldrich and deionized water was used as the solvent.

### 2.2. Synthesis of $Co_xFe_{3-x}O_4$ nanoparticles

Cobalt-ferrite nanoparticles ($Co_xFe_{3-x}O_4$) were synthesized by a hydrothermal method. CTAB was diluted in 17 ml of deionized water and stirred for 15 minutes. Co $(NO_3)_2$-$6H_2O$ was then added and the mixture was stirred for a further 15 minutes. Finally, Fe $(NO_3)_3$-$9H_2O$ was added to the solution. The quantities of Co and Fe nitrates were calculated to obtain the required Co/Fe atomic ratios for x = 1 and x = 1.5 and 1.5g as a total mass of precursors. The pH of solution was adjusted to 12 by gradual addition of 12 ml of 1 M NaOH solution. The mixture was stirred for 30 minutes at room temperature [19, 20]. The resulting solution was transferred to a teflon reactor and loaded into an autoclave for heat treatment of 24 hours at 160°C. The resultant precipitate was rinsed several times using deionized water followed by ethanol until the pH value was stable. The precipitate finally dried at 80°C for 10 hours.

### 2.3. Characterization techniques

The X-ray diffraction (XRD) characterization was performed on the samples using Empyrean Panalytical diffractometer with a Cu-Kα beam source (wavelength λ = 1.54 Å). The XRD patterns were registered in the range of 2θ from 10° to 80° with step size of 0.02° at a scan rate of 1°/ minutes. The specific surface area of the $Co_xFe_{3-x}O_4$ has been determined thanks to $N_2$ adsorption-desorption isotherm at 77 K (Autosorb-iQ, Quantachrome, USA). A 200 kV FEI Tecnai G2 transmission electron microscope coupled with an energy dispersive spectrometer (EDS) were used for both conventional high-resolution images of the grains and chemical composition investigations. These characterizations provided a view of the size distribution, crystalline structure, morphology, and chemical homogeneity of the $Co_xFe_{3-x}O_4$ particles.

The optical properties of the particles were obtained thanks to a Shimadzu UV-1800 spectrophotometer with diffuse reflectance mode (DRS). The absorption spectra of the Rhodamine B (RhB) dye used to evaluated the photocatalytic performance were collected in the wavelength range 200-800 nm using a UV-visible spectrophotometer [21].

The fluorescence (FL) and time resolved fluorescence emission (TRFL) decay studies were performed using a Fluoromax (Horiba) fluorescence spectrophotometer. The excitation wavelength was chosen to be 310 nm, and the emission wavelength to be 465 nm. The decay curves were fitted with a biexponential function according to Equation (1) [22]:

$$I_t = I_1 e^{-(t/\tau_1)} + I_2 e^{-(t/\tau_2)} \qquad (1)$$

where $I_1$ and $I_2$ are the intensities at different times of the decay and $\tau_1$ and $\tau_2$ are their respective lifetimes. The carrier lifetime $\tau_{moy}$ was extracted using Equation (2) [23] :

$$\tau_{moy} = \frac{(I_1\tau_1^2 + I_2\tau_2^2)}{(I_1\tau_1 + I_2\tau_2)} \qquad (2)$$

2.4. Photoelectrochemical Measurements

The photoelectrochemical studies were carried out using an OrigaLys electrochemical workstation equipped with a system of three electrodes. The reference and counter electrodes were an Ag/AgCl electrode and a platinum foil, respectively. The working electrodes (WE) were made by depositing the synthesized photocatalyst material on indium tin oxide substrates (ITO) by drop casting method. The electrochemical and photoelectrochemical measurements were performed in aqueous electrolyte solution of 0.1 M sodium sulphate ($Na_2SO_4$). The irradiation setup was a revoler Instytut Fotonowy LED, it allows accurate control of the incident light wavelength. When a photocatalytic material is exposed to light, charge carriers are created (electrons and holes). The photocurrent technique measures the electrical current generated, provides information about the separation of

charge carriers and the recombination dynamics. The measurements were recorded under the applied potential of 1.2 V which was chosen to guarantee a stable and measurable current signal. Complementary to photocurrent analysis, electrochemical impedance spectroscopy (EIS) was conducted to study the charge transfer resistance given by the Nyquist plot. EIS measurement was carried out with a three-electrode system in which a 5 mV AC signal was applied at the working electrode over a frequency range of 0.01 Hz to 100 kHz. Mott-Schottky experiments were also carried out to measure the electrochemical capacitance of the photocatalyst versus applied potential at a fixed frequency of 500 Hz. By plotting the inverse square of the capacitance against the applied potential, flat-band potential and charge carrier density were extracted, providing valuable understanding on the semiconductor-type behavior of the $Co_xFe_{3-x}O_4$ ferrite.

### 2.5. Photocatalytic Set-up

To evaluate the photocatalytic behavior of the ferrite, we studied the photodegradation of Rhodamine B (RhB) under Simulated Sunlight. For the measurements, several RhB solutions with concentration between 5 and 15 ppm and quantities of catalyst material from 50 to 100 mg were used. In a first step, before exposure, the RhB solution with the ferrite was agitated for one hour to establish an adsorption/desorption equilibrium between the Rhodamine B molecules and the surface of the photocatalyst. To study the effect of the pH on the photodegradation performance, experiments were performed at different pH values, typically ranging from 5 to 9. Note that pH affects the ionization of functional groups on the surface, such as hydroxyl groups, which influences the overall charge of the catalyst. During the photodegradation reaction, 3 ml of the solution were taken at various times to follow the variation of the RhB concentration thanks to changes in the intensity of absorption peaks. The main absorption band of RhB is known to be at 554 nm which was used as the reference wavelength for the measurement of the dye concentration, the spectra were collected with a Shimadzu UV-1800 Spectrophotometer. Total organic carbon (TOC) analyses allowed to determine the organic carbon content of polluted solution. By comparing the initial value with that obtained after photodegradation, it is possible to estimate the mineralization of rhodamine molecules. The percentage of TOC removal was calculated using the initial and final TOC values according to the formula:

$$\text{TOC removal (\%)} = \frac{TOC_i - TOC_f}{TOC_i} \times 100 \qquad (3)$$

Where $TOC_i$ is the measured value for initial solution and $TOC_f$ represent the measured value after the photodegradation process.

### 2.6. BBD-RSM design and data analysis

The optimization of parameters for the removal of Rhodamine B has been performed using the Box-Behnken design (RSM-BBD), based on statistical approach. This methodology is aimed not only to determine the optimum conditions for maximum photodegradation, but also to assess high degradation rates with minimal catalyst amount and higher RhB concentrations. In addition, RSM-BBD is used to analyze the effects of interactions between the factors (experimental parameters) [24,25]. In this factorial design, 3-factors and 3-level model (low (-1), medium (0), and high (+1)) were used which leads to a basic BBD cubic structure [26]. This model involves 17 experiments corresponding to 12 factorial tests and 5 center tests. The results of the 17 experiments were exploited using NemrodW software, a quadratic polynomial equation correlates the factors to the Y predicted response (Y = % RhB photodegradation) Equation (4) [25]:

$$Y = b_0 + \sum_{i=1}^{k} b_i x_i + \sum_{i=1}^{k} b_{i-i} x_i^2 + \sum_{i=1}^{k-1} \sum_{j=i+1}^{k} b_{i-j}\, x_i x_j + \varepsilon \quad (4)$$

Where k is number of factors, $b_i$ and $b_{i-i}$ represent, respectively, the linear effects and the quadratic term of the $X_i$ independent variables, $b_{i-j}$ shows the interaction effects between different pairs of $X_i$ $X_j$ variables, ε is the model error and $b_0$ the model coefficient. To compare the effects of the variable's, coded variables are defined according to the following Equation (5).

$$x_i = \frac{X_i - X_{io}}{\delta X_i} \quad (5)$$

Where $\mathbf{x_i}$ is the coded variable of $X_i$ real variable, $X_{i0}$ = value of $X_i$ at the center point and $\delta X_i$ is the variation step of $X_i$. Equation 4 highlights the relationships between experimental parameters, revealing synergistic or antagonistic effects. The choice of factors was based on literature related to organic dyes degradation and initial laboratory experiments. Table 1 shows the range of experimental values of the parameters and their corresponding levels.

**Table 1:** Experimental range and levels in the BBD Model.

| Factor | Levels | | |
|---|---|---|---|
| | -1 | 0 | +1 |
| $X_1$: pH | 5 | 7 | 9 |
| $X_2$: [$RhB_0$] (ppm) | 5 | 10 | 15 |
| $X_3$: Amount of catalyst (mg) | 50 | 75 | 100 |

Coefficients of regression associated with each term in the model were estimated using response surface methodology. The significance of model variables has been evaluated using Analysis of Variance (ANOVA), with a 95% confidence level as the test criterion Three-dimensional (3D) response surfaces and two-dimensional (2D) contour plots were generated thanks to the response models. These plots allowed the prediction of the degradation rates for different combinations of

parameters, thereby determining the optimal conditions for achieving maximum Rhodamine B photodegradation efficiency.

## 3. Results and discussion

### 3.1. XRD analysis of $Co_xFe_{3-x}O_4$ nanoparticles

The XRD patterns of the $CoFe_2O_4$ and $Co_{1.5}Fe_{1.5}O_4$ nanoparticles (Fig. 1) show a single-phased spinel structure with a space group (Fd-3 m) and no additional peaks. The observed diffraction peaks at 2θ values of 18.38°, 30.35°, 35.66°, 37.14°, 43.18°, 53.58°, 57.08°, 62.75° and 74.71°, correspond to (111), (220), (311), (222), (400), (422), (511), (440) and (533) planes respectively, are in good agreement with the standard JCPDS No. 22-1086 [27] of $CoFe_2O_4$ structure. The observed shift of XRD peaks towards higher angles for $Co_{1.5}Fe_{1.5}O_4$ compared to $CoFe_2O_4$ is due to the change in the lattice parameters [20]. Indeed, for x = 1.5 there is more substitution of $Fe^{3+}$ ions by $Co^{2+}$ ions, which having a smaller ionic radius, gives a reduction of the lattice parameter. The average crystallite size, estimated from the XRD data using the Scherrer equation, shows a slight decrease with the cobalt content increases: from 9 nm for $CoFe_2O_4$ to 7 nm for $Co_{1.5}Fe_{1.5}O_4$, in agreement with the literature [28].

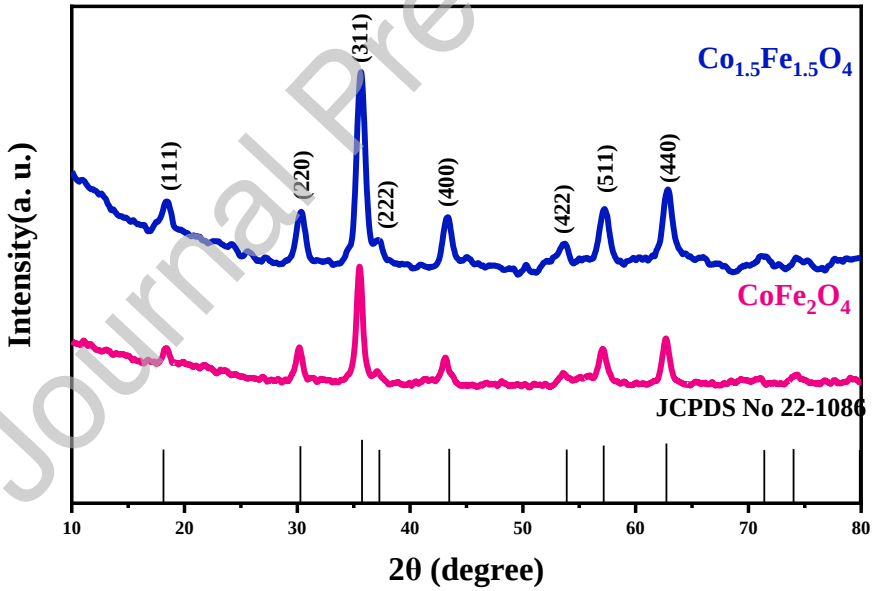


**Fig. 1.** X-ray diffraction patterns of $Co_xFe_{3-x}O_4$ samples with x= 1 (pink) and x=1.5 (blue).

### 3.2. Surface morphology and BET Analysis.

The transmission electron microscopy (TEM) provides an overview of the nanoparticles (size, morphology) and allows thanks to the energy dispersive spectroscopy associated, to determine their chemical composition [29]. TEM images (Fig. 2.a and 2.b) reveal faceted and polygonal shapes which suggest nano-octahedral morphologies for both compositions $CoFe_2O_4$ and $Co_{1.5}Fe_{1.5}O_4$. It is important to note that the TEM images represent 2D projections of the nanoparticles, and due to the

viewing angle, their octahedral morphology may not be immediately apparent in all cases. Fig. 2.d. clearly illustrates the different projections of an octahedron observed along various axes [19]. From size measurements on the TEM images, size distribution histograms were plotted (Fig. 2.a' and 2.b'), leading to an average size of approximately 9 nm for $CoFe_2O_4$ and a slightly smaller size of 8 nm for $Co_{1.5}Fe_{1.5}O_4$. The selected area electronic diffraction patterns (one example Fig. 2.c) were obtained from several nanoparticles. They have the same appearance for both compositions and exhibit punctuated rings corresponding to the plans of the spinel structure [27] in Bragg position. The slight decrease in the cell parameter due to the increase in the cobalt rate, observed by XRD, is not measurable on this type of pattern.

The EDS spectra (reported in S1) show the different emission peaks of O, Fe, and Co. The atomic percent of each element is given from the peak deconvolution. In this study, we focused on the Fe/Co ratio which allows to determine the x value in $Co_xFe_{3-x}O_4$ phases. For each composition, several analyses were carried out and give the following values 0.92 ± 0.08 for $CoFe_2O_4$ and 1.42 ± 0.07 for $Co_{1.5}Fe_{1.5}O_4$, which is in good agreement with the expected one.

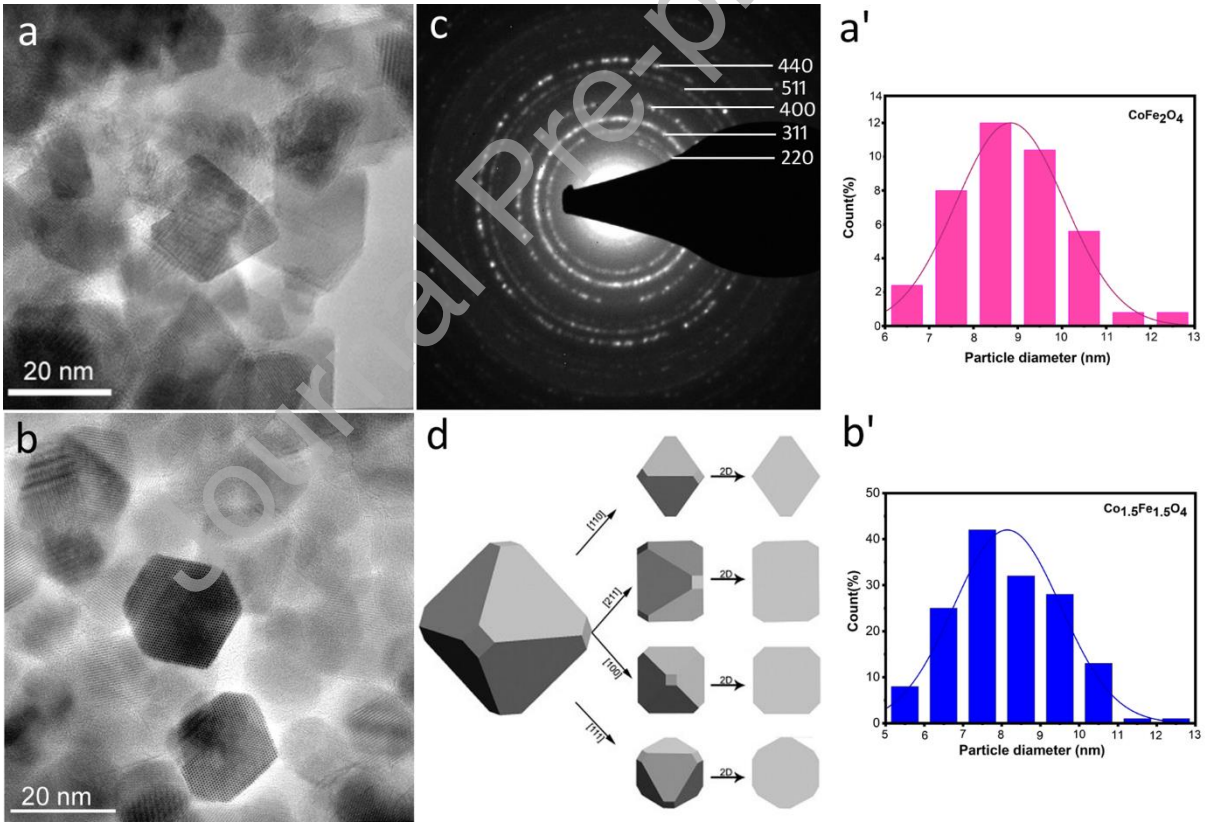


**Fig. 2.** TEM micrographs of (a) $CoFe_2O_4$, (b) $Co_{1.5}Fe_{1.5}O_4$ and the size distribution (a') $CoFe_2O_4$, (b') $Co_{1.5}Fe_{1.5}O_4$, c) Selected area electronic diffraction pattern of $CoFe_2O_4$, d) 3D and 2D aspect of an octahedron viewed along different directions [19].

The Brunauer-Emmett Teller (BET) method offers an approach to explain the adsorption phenomenon in which gas molecules adsorbed to the surface of materials [30]. The BET technique is widely used to measure the specific surface area by examining the adsorption behavior of gas molecule on the surface of a solid [31].

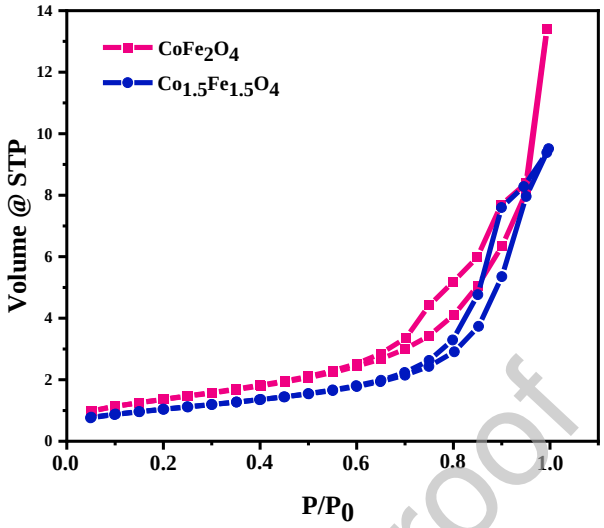


**Fig. 3**. $N_2$ adsorption/desorption isotherms of $CoFe_2O_4$ (pink) and $Co_{1.5}Fe_{1.5}O_4$ (blue).

The nitrogen adsorption-desorption isotherms for both $CoFe_2O_4$ and $Co_{1.5}Fe_{1.5}O_4$ nanoparticles (Fig. 3) exhibit a IV type with a clear H3 type hysteresis loop, between the adsorption and desorption branches, according to the classification of the International Union of Pure and Applied Chemistry (IUPAC) [32]. This hysteresis loop indicates the presence of mesoporous textural porosity [33,34]. The results of BET measurements indicate that for the two compositions, nanoparticles exhibit comparable specific surface areas (102 $m^2/g$ for $CoFe_2O_4$ and 106 $m^2/g$ for $Co_{1.5}Fe_{1.5}O_4$) which are significantly high compared to the values reported for $CoFe_2O_4$ nanoparticles prepared with other methods, which are typically in the range of 40-90 $m^2/g$ [35,36] and this suggest that the two materials have similar availability of surface sites for adsorption.

### 3.3. Optical property

The optical properties of cobalt ferrite $Co_xFe_{3-x}O_4$ (x = 1 and 1.5) were investigated using UV-vis diffuse reflectance spectroscopy which makes it possible to obtain their band gap energy (Eg). The Kubelka-Munk function F(R) was first applied to convert the reflectance (R) data into absorption spectra. In a second step, Tauc's Equation (6) was used to extract the band gap energy values from the absorption spectra by plotting $(F(R)h\nu)^{1/\gamma}$ versus hν [37] (Fig. 4):

$$(\alpha h\nu)^{1/\gamma} = B\left(h\nu - E_g\right) \qquad (6)$$

where α represents the absorption coefficient, h the Planck constant, ν the frequency of the photon and γ is equal to 1/2 for direct band gaps and 2 for indirect band gaps [38]. Several studies have indicated a direct band gap for $CoFe_2O_4$ [39,40]. The bandgap energy corresponds to the intersection of the extrapolated line segment of the curve and the energy axis. The obtained $E_g$ values for $CoFe_2O_4$ and $Co_{1.5}Fe_{1.5}O_4$ were found to be 2.32 eV and 2.18 eV respectively (Fig. 4), indicating that both materials absorb visible light and therefore are active in the visible range. In $CoFe_2O_4$ spinel, the valence band (VB) is predominantly given by the oxygen 2p orbitals with a contribution of 3d orbitals of $Fe^{3+}$, on another side, the conduction band (CB) is composed of $Co^{2+}$ and $Fe^{3+}$ 3d orbitals [41]. In $Co_{1.5}Fe_{1.5}O_4$, as the cobalt content increases, most $Co^{2+}$ ions occupy the B (octahedral) sites of the spinel structure, altering the electronic interaction between $Co^{2+}$ and $Fe^{3+}$ ions. The introduction of additional $Co^{2+}$ cations change the distribution of d-orbital energies, reducing the energy difference between the VB and CB [42], this is what is observed in the experimental results: a decrease of the bandgap energy.

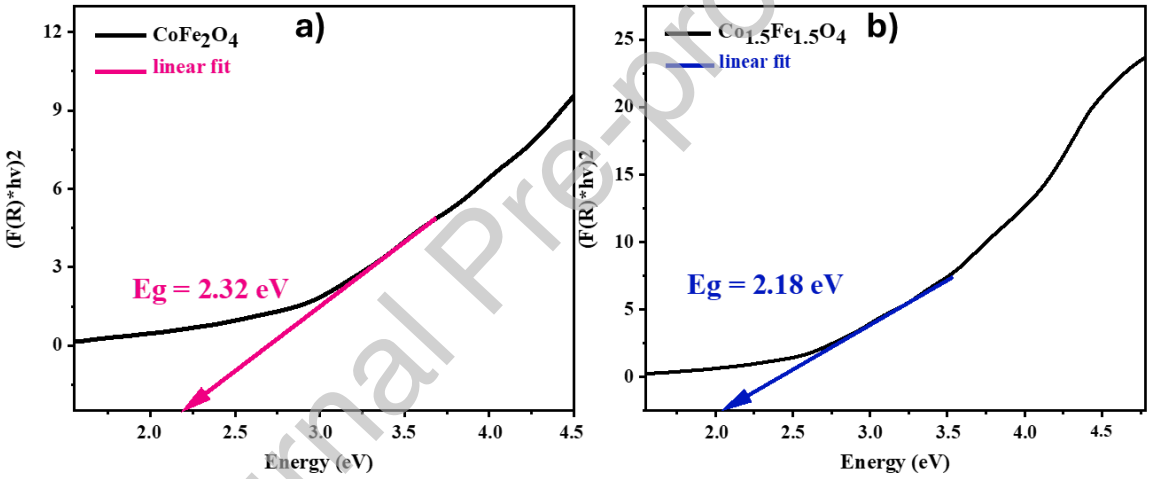


**Fig. 4.** Tauc plots of a) $CoFe_2O_4$ and b) $Co_{1.5}Fe_{1.5}O_4$.

### 3.4. Photo-electrochemical measurements

Photocurrent measurements are essential to understand the photocatalytic degradation of dyes, since they give insights into the photo-generation of charge carriers, such as electron-hole pairs. Electrochemical impedance spectroscopy (EIS) leads to study the resistance to charge transfer. The EIS results are usually presented as Nyquist plots which typically show semicircular arcs given by imaginary part of impedance (Z″) versus the real part (Z′). It is well known that the diameter of the arc is related to the resistance to charge transfer (Rct) [43]. Fig. 5.a. represents the Nyquist plots obtained for the two ferrite compositions ($CoFe_2O_4$ and $Co_{1.5}Fe_{1.5}O_4$). The curves are very similar, displaying a semicircular portion typical of charge transfer resistance (Rct). However, the size of the semi-circles in both materials is quite different. The $CoFe_2O_4$ catalyst shows a large semicircle indicating a high Rct value of 3.3 kΩ/cm² which is obtained from fitting the EIS data to an equivalent

circuit model. This large semicircle indicates more resistance to charge movement at the electrode-electrolyte interface, implying that the charge transfer process is slower compared to the x=1.5 composition. In fact, $Co_{1.5}Fe_{1.5}O_4$ exhibits a smaller semicircle, which corresponds to a lower Rct of 2.8 kΩ/cm². The lower Rct reflected an enhanced charge transfer mechanism, which indicates that the addition of cobalt improves the separation of photogenerated electron-hole pairs and facilitates faster charge movement across the interface [44].

The photocurrent response is a complementary study since it provides useful information on the separation of photo-generated carriers in semiconductor materials [45,46]. Fig. 5.b, shows the photocurrent response of indium tin oxide (ITO), $CoFe_2O_4$ and $Co_{1.5}Fe_{1.5}O_4$ under 390 nm wavelength at an applied voltage of 1.2V. The 390 nm wavelength was chosen because it is close to the visible region of the spectrum and allows for a significant photocurrent response. Also, the choice of 1.2 V vs. RHE as the applied potential is essential to ensure a positive photocurrent generation. ITO, which is used as substrate, shows negligible photocurrent, confirming its lack of photoactivity. In contrast, $CoFe_2O_4$ generates a moderate photocurrent of 0.75 µA/cm$^2$ during the light-on period, indicating its ability to absorb light and produce electron-hole pairs. At the same time, $Co_{1.5}Fe_{1.5}O_4$ shows a higher photocurrent density of 1.18 µA/cm², indicating that the increase in cobalt level in the ferrite enhances charge carrier generation. During the illumination time, the value of each photocurrent is stable, which indicates an efficient charge separation and transport leading to lower recombination rate. The higher photocurrent intensity in $Co_{1.5}Fe_{1.5}O_4$ indicates that it is a potential more effective material for photoelectrochemical applications compared to $CoFe_2O_4$.

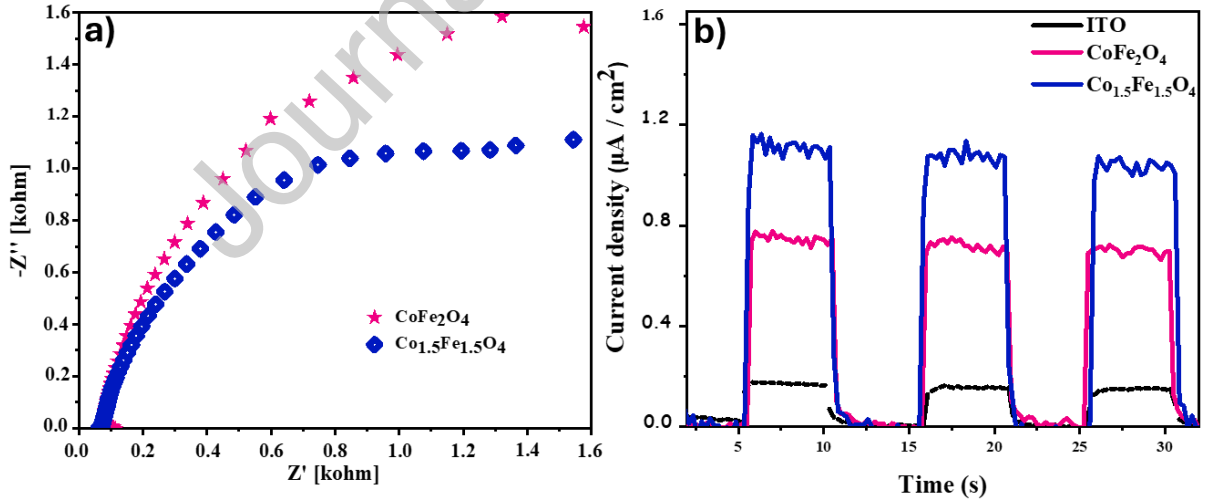


**Fig. 5.** (a) EIS graphs and (b) The transient photocurrent curves of ITO (black), $CoFe_2O_4$ (pink) and $Co_{1.5}Fe_{1.5}O_4$ (blue).

3.5. Optimization of parameters using response surface methodology

In this study, the influence of three experimental parameters process on rhodamine B photodegradation efficiency was investigated using $CoFe_2O_4$ as catalyst. These parameters were pH ($X_1$) and initial RhB concentration ($X_2$) of the polluted solution and mass of photocatalyst ($X_3$); for each of these factors, three values were tested (low (-1), medium (0), and high (+1)). A total of 17 experiments were conducted to investigate the effect of the three independent factors on the RhB degradation rate and their interactions [47]. Table 2 presents the complete matrix of the experimental design of the three variables studied, and the measured/expected responses i.e. Rhodamine B degradation efficiencies (%). Multiple regression analysis of the experimental data, with coded values, was obtained from the following Equation (7) [48] :

$$Y = 86.66 + 13.66\,x_1 - 6.17\,x_2 + 7.35\,x_3 - 8.69\,x_1^2 - 5.06\,x_2^2 + 6.25\,x_3^2 - 0.17\,x_1x_2 - 2.92\,x_1x_3 + 3.88\,x_2x_3 \qquad (7)$$

Table 3 shows the results of the ANOVA (Analysis of Variance) employed to evaluate the statistical significance of the regression models developed and to determine the effect of the terms (linear, quadratic and interactions terms) on the response variable [16,49]. The correlation between the predicted and experimental value is supported by the values of $R^2 = 0.99$ and adjusted $R^2 = 0.98$. The significance of the value of the coefficient was evaluated using the p-value, which must be inferior to 5% [49]. The results (Table 3) reveal that the individual factors pH ($X_1$), initial RhB concentration ($X_2$) and catalyst amount ($X_3$), as well as their quadratic terms ($X_1^2$, $X_2^2$, $X_3^2$) and the interaction terms $X_1X_3$ and $X_2X_3$, are significant, as can be seen from their p-values under 0.05. However, the effect of the interaction between pH and initial RhB concentration ($X_1X_2$) is found not to be significant, with a p value of 42.50.

**Table 2**: Design matrix for three variables with experimental and predicted responses using $CoFe_2O_4$.

| | pH | RhB (ppm) | Amount of catalyst(mg) | Experimental Removal (%) | Predicted Removal (%) | Residues |
|---|---|---|---|---|---|---|
| **1** | 5 | 5 | 75 | 63.03 | 65.25 | -2.22 |
| **2** | 9 | 5 | 75 | 93.66 | 92.91 | 0.75 |
| **3** | 5 | 15 | 75 | 52.51 | 53.26 | -0.75 |
| **4** | 9 | 15 | 75 | 82.46 | 80.24 | 2.22 |
| **5** | 5 | 10 | 50 | 62.67 | 60.30 | 2.37 |
| **6** | 9 | 10 | 50 | 92.86 | 93.46 | -0.60 |
| **7** | 5 | 10 | 100 | 81.44 | 80.84 | 0.60 |
| **8** | 9 | 10 | 100 | 99.95 | 102.32 | -2.37 |
| **9** | 7 | 5 | 50 | 90.41 | 90.56 | -0.15 |

| | | | | | | |
|---|---|---|---|---|---|---|
| **10** | 7 | 15 | 50 | 68.84 | 70.46 | -1.62 |
| **11** | 7 | 5 | 100 | 99.11 | 97.49 | 1.62 |
| **12** | 7 | 15 | 100 | 93.07 | 92.92 | 0.15 |
| **13** | 7 | 10 | 75 | 86.05 | 86.54 | -0.49 |
| **14** | 7 | 10 | 75 | 86.30 | 86.54 | -0.24 |
| **15** | 7 | 10 | 75 | 86.78 | 86.54 | 0.24 |
| **16** | 7 | 10 | 75 | 87.02 | 86.54 | 0.48 |
| **17** | 7 | 10 | 75 | 86.56 | 86.54 | 0.02 |

From the analysis of the $b_i$ and $b_{i-j}$ coefficients (Table 3**)** the respective influence of the different parameters on the response can be estimated. A positive coefficient means that the corresponding parameter has a positive effect on the photodegradation. Conversely, negative value leads to an antagonistic effect on the process. The highest value of the $b_i$ coefficient is obtained for the pH parameter ($b_1$), indicating that pH has the strongest positive influence on photocatalytic performance compared to the initial RhB concentration ($b_2$) and the catalyst amount ($b_3$). This is supported by the experimental results see Table 2. For example, in experiment 3, with 15 ppm of RhB, at pH 5, and 75 mg of catalyst, the degradation efficiency was 53%. When the pH was increased to 9 (Experiment 4), the photodegradation efficiency increased significantly to reach 82%, which represents an enhancement of 57%. Increasing the catalyst amount from 50 mg to 100 mg improved the degradation rate only by 30% (Experiments 5 to 7), while increasing the RhB concentration from 5 ppm to 15 ppm reduced it by 16% (Experiments 1 to 3). A ($b_{i-i}$) positive quadratic coefficient means that the parameter follows a linear variation, if it is negative, this means that it shows a maximum value in response within selected ranges of parameters [50]. The negative quadratic coefficient for pH ($b_{1-1}$) and rhodamine concentration ($b_{2-2}$) indicate that within the range of selected values, the response passes through a maximum for these 2 parameters. Regarding the amount of catalyst, the ($b_{3-3}$) coefficient is linear, which was to be expected: for a given pH and pollutant concentration, the percentage of degradation increases with the mass. At the level of the interaction terms, only the ($b_{2-3}$) coefficient is positive reflecting a synergistic effect between the concentration of RhB and the amount of catalyst. A simultaneous increase of RhB concentration and catalyst amount increases the degradation rate.

**Table 3:** Results of Analysis of variance ANOVA using $CoFe_2O_4$ as a catalyst.

| Source | Coefficient | Ecart-type | p-value |
|---|---|---|---|
| **Model** | | - | |
| **b0** | 86.54 | 0,17 | <0,01 |
| **b1** | 13.66 | 0,13 | <0,01 |

| | | | |
|---|---|---|---|
| **b2** | -6.17 | 0,13 | <0,01 |
| **b3** | 7.35 | 0,13 | <0,01 |
| **b1-1** | -8.63 | 0,18 | <0,01 |
| **b2-2** | -5.00 | 0,18 | <0,01 |
| **b3-3** | 6.32 | 0,18 | <0,01 |
| **b1-2** | -0.17 | 0,19 | 42.5 |
| **b1-3** | -2.92 | 0,19 | <0,01 |
| **b2-3** | 3.88 | 0,19 | <0,01 |
| $R^2$ | | 0.99 | |
| **Adj.**$R^2$ | | 0.98 | |

To visualize the results, the response model can be represented by 2D contours and 3D response surface plots, which allow to analyze the behavior of two parameters while the third is fixed (Fig. 6). In the 3D response surface, we plot the % degradation as a function of two factors, in addition the 2D contour plots represent a projection of the direct relationship between these two factors. Together, they provide a more complete picture of the interaction of variables, pairwise, to guide experimental design and process optimization of the decomposition [49]. Fig. 6a. shows the behavior of the [$RhB_0$]/catalyst amount pair corresponding to the highest value of bi-j coefficient, the maximum degradation is obtained for pH = 9. In the same way for the pH/ catalyst amount pair, a maximum degradation rate could be determined (10 ppm of [RhB]). However, in the case of the pH/[$RhB_0$] pair, the maximum is not reached over the range of values studied, this would occur for pH values of less than 5 or greater than 9. By using Nemrodw software and 3D plots, it is possible to predict the values of degradation for any set of parameters. The predicted value of the complete photodegradation of RhB (100%), was achieved with a catalyst dosage of 95 mg, a pH of 9 and a Rhodamine B concentration of 10 mg/L, demonstrating excellent agreement with the prediction. However, under non-optimal conditions, as in Experiment 6 (pH = 9, 10 ppm RhB, and 50 mg of catalyst, which is nearly half of the optimal amount of 95 mg), the efficiency of degradation only decreased slightly by 7 %, achieving a degradation of 93%. From a practical and economic point of view, this last configuration, which gives an honorable rate of degradation, seems to be a better alternative since it consumes half as much catalyst mass. These findings indicate that a higher degradation rate can be obtained with a significantly reduced amount of catalyst, thus highlighting the efficiency and practicality of the optimized conditions.

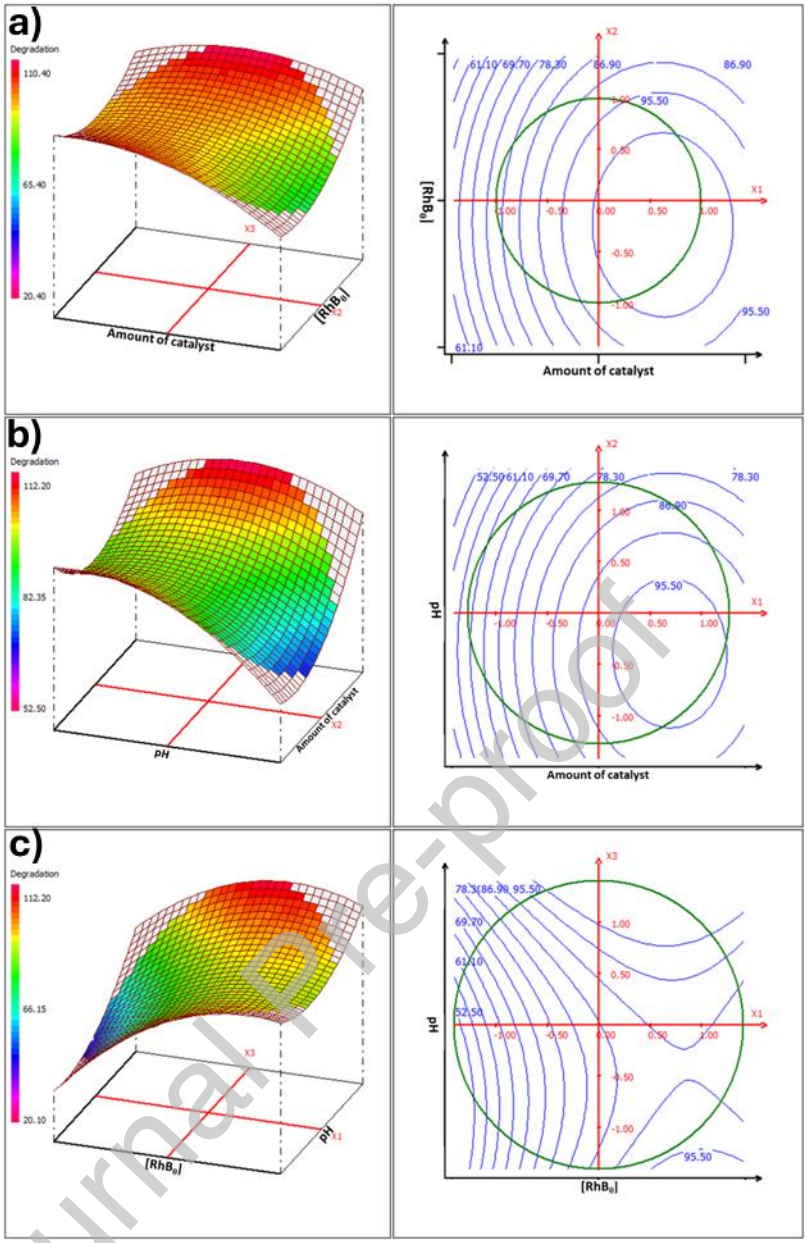


**Fig. 6.** The 3D response surface plots and 2D contour plots of **(a)** RhB concentration and amount of catalyst **(b)** pH and amount of catalyst **(c)**, pH and RhB concentration.

### 3.6. Photocatalytic activity of $Co_xFe_{3-x}O_4$

#### 3.6.1. Adsorption and photolysis investigation

To investigate the contribution of adsorption to the degradation of Rhodamine B, dark adsorption experiments were performed on $CoFe_2O_4$ photocatalysts. Fig. 7.a shows the UV-visible absorption spectra of the polluted solution as a function of time where the principal peak at 554 nm is characteristic of the RhB molecules. The decrease in absorbance of the characteristic peak over time shows the decrease in RhB concentration in the presence of $CoFe_2O_4$ catalyst. As can be seen after 30 min, all curves overlap which means that the adsorption-desorption equilibrium is reached. The absorption of RhB decreased by 10% and stabilized after 30 min. This result indicates a negligible

adsorption capacity for the as-synthesized cobalt ferrites. Complementary photolysis experiments (Fig. 7.b) performed under solar light irradiation in the absence of catalysts with an initial concentration of 10 ppm showed a reduction in RhB concentration of only 8% after 240 min. These findings indicate that the removal of RhB during the illumination process is mainly due to photocatalytic mechanism rather than physical adsorption or direct photolytic pathways.

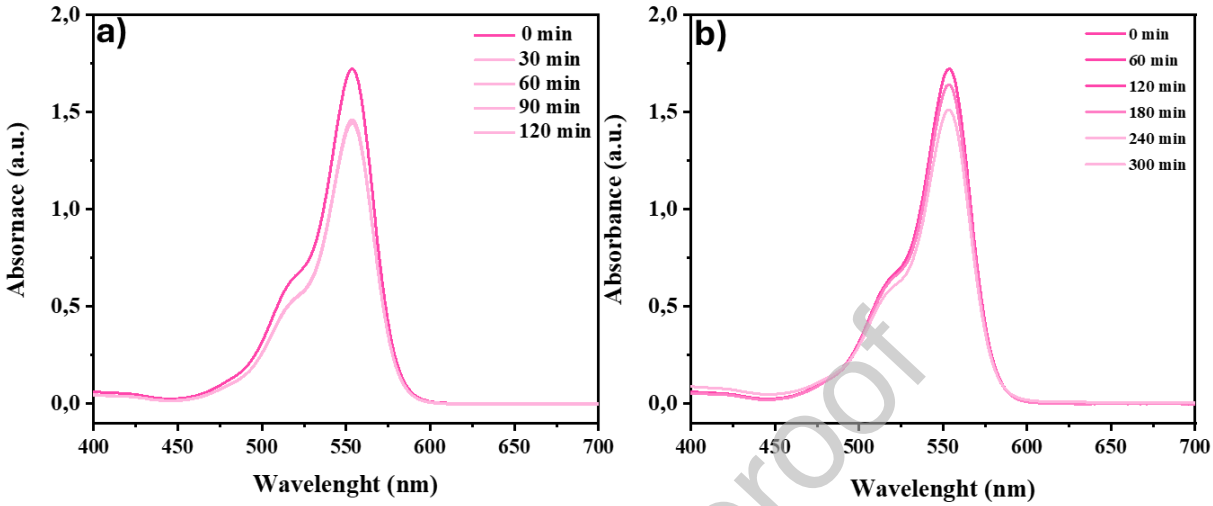


**Fig. 7.** UV-visible spectra of polluted solution (a) in absence of light and (b) in absence of catalyst.

### 3.6.2. Photocatalytic activity of $CoFe_2O_4$ and $Co_{1.5}Fe_{1.5}O_4$

The photocatalytic experiments were carried out under the optimum conditions determined above for $CoFe_2O_4$. The activity of $Co_{1.5}Fe_{1.5}O_4$ has been investigated under the same conditions to be compared to the first one. Fig 8.a represents the UV-visible absorption spectra of the polluted solution collected at different time intervals. The decrease in absorbance of the characteristic peak of 554 nm over time shows the progressive decrease of RhB dye concentration in the presence of $CoFe_2O_4$ catalyst during the irradiation. From the absorption spectra, it is possible to calculate the ratio $Ct/C_0$ ($C_t$ = RhB concentration of the solution at the time of the measurement, $C_o$= RhB concentration of the initial solution). Fig. 8.b shows the ($C_t/C_0$) of the polluted solution versus time plot for $CoFe_2O_4$ and $Co_{1.5}Fe_{1.5}O_4$, as well as the photolysis process. Photolysis (photodegradation of RhB in the absence of a catalyst) experiment showed a minor decrease in dye concentration, which emphasizes the crucial importance of both catalysts in facilitating the photodegradation process. For both catalysts, a similar trend can be observed, with a rapid decrease of RhB concentration in the first 100 minutes, followed by a slower decrease. 100 % of RhB was degraded in 180 minutes over $Co_{1.5}Fe_{1.5}O_4$ photocatalyst, whereas $CoFe_2O_4$ required 240 minutes to reach the same level of RhB degradation.

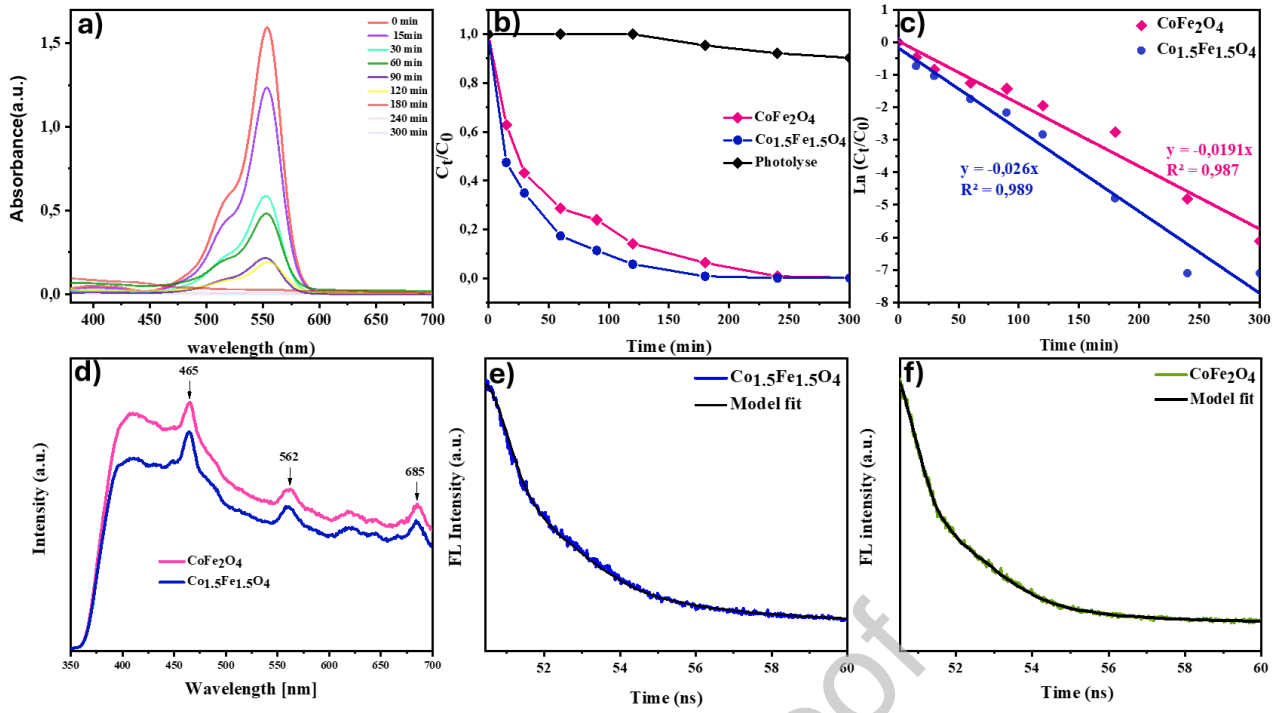


**Fig. 8. (**a) Evolution over the time of the UV-vis absorption spectra of RhB solution in presence of $CoFe_2O_4$. (b) $C_t/C_0$ evolution as function of time for photolysis, $CoFe_2O_4$ and $Co_{1.5}Fe_{1.5}O_4$. (c) Pseudo-first order kinetic model of the photocatalytic degradation rate of the dye Rhodamine B. (d) Fluorescence Spectra and (e-f) Time-resolved fluorescence lifetime spectra of $CoFe_2O_4$ and $Co_{1.5}Fe_{1.5}O_4$.

To complete the comparison of the two samples, a first-order kinetic model was used for the kinetic analysis of the degradation process, as illustrated in Fig. 8.c, where the logarithm of the concentration ratio $C_t/C_0$ is plotted against time. The kinetic constant for $CoFe_2O_4$ was obtained to be k = -0.019 $minutes^{-1}$, while a higher rate constant of k = -0.025 $minutes^{-1}$ was measured for $Co_{1.5}Fe_{1.5}O_4$. These results indicate that $Co_{1.5}Fe_{1.5}O_4$ degrades RhB more quickly than $CoFe_2O_4$.

To better understand the charge carrier dynamics, fluorescence spectroscopy measurements were performed. The fluorescent patterns give essential information about the carrier lifetime and recombination of electron-hole pairs in the catalyst materials. Fig. 8.d presents the fluorescence spectra of the two catalysts, they exhibit similar peaks at the same wavelength but with different intensities. $CoFe_2O_4$ has a higher fluorescence intensity than $Co_{1.5}Fe_{1.5}O_4$, this intensity is usually correlated to the rate of carrier recombination So for x=1 there is more electron-hole recombination than for x=1.5 thus reducing the availability of carriers to participate in photocatalytic reactions [51–53]. The lower recombination rate results in longer carrier lifetimes. As shown in Fig. 8.e and 8.f, the lifetime of charge carriers was determined by time-resolved fluorescence lifetime spectroscopy, for $Co_{1.5}Fe_{1.5}O_4$, is about 5.2 ns, while for $CoFe_2O_4$ they have a shorter lifetime of about 2.9 ns. The longer lifetime for x=1.5 means that there are more electrons and holes present to participate in the photocatalytic reactions. The increase in lifetime is linked to the higher cobalt content, which, as we mentioned above, induces a reduction of the lattice parameters and the band gap energy.

Consequently, in the lattice there is polyhedral distortion which can modify the electronic band structure. This acts as an electron trap and slows down recombination [54], and facilitates diffusion of charge on the surface, which promotes charge separation.

3.6.3. Radical trapping tests

To identify the principal reactive chemical species responsible for dyes degradation, radical trapping studies were carried out. L-ascorbic acid (L-asc), ethylene-diamine-tetra-acetic acid disodium (EDTA) and isopropyl alcohol (IPA) were used as specific scavengers for ($O_2^{\bullet-}$) superoxide radicals, ($h^+$) holes and ($OH^\bullet$) hydroxyl radicals, respectively [55–57]. During the tests, a lower degradation rate indicates that the trapped species being tested is more active in the degradation mechanism.

Fig. 9.a illustrates the RhB degradation efficiency in the presence of different trapping agents when $CoFe_2O_4$ and $Co_{1.5}Fe_{1.5}O_4$ are used as photocatalysts. The measurements were taken after 180 minutes which corresponds to the time required for complete degradation for x=1.5. Both plots display a similar trend over the different trapping tests, which indicates that the reactive species responsible for the reactions are operating in a common way. $Co_{1.5}Fe_{1.5}O_4$ exhibits a superior photocatalytic activity (100% degradation without scavenger), and for $CoFe_2O_4$ it is a little weaker (90%). It should be remembered that the complete degradation for x=1 is obtained after 240 minutes. The introduction of specific trapping agents led to more or less important modification of the degradation efficiency. The addition of isopropyl alcohol (IPA), a trapping agent for hydroxyl radicals ($OH^\bullet$), significantly decreased the degradation rate to 21%, emphasizing the crucial role of hydroxyl radicals as a major oxidizing species in the process. In addition, EDTA, a scavenger for holes ($h^+$), also caused a significant decrease of the degradation rate to 24%, highlighting the role of holes in the photocatalytic pathway. Furthermore, the addition of L-ascorbic acid, an $O_2^{\bullet-}$ scavenger, decreased the degradation rate to 82%, which suggests that the superoxide species contribution is relatively minor when compared to hydroxyl radicals and holes. The same trend and the same involvement of reactive species were observed for $CoFe_2O_4$, the different specific efficiency values resulting from the longer reaction time previously discussed.

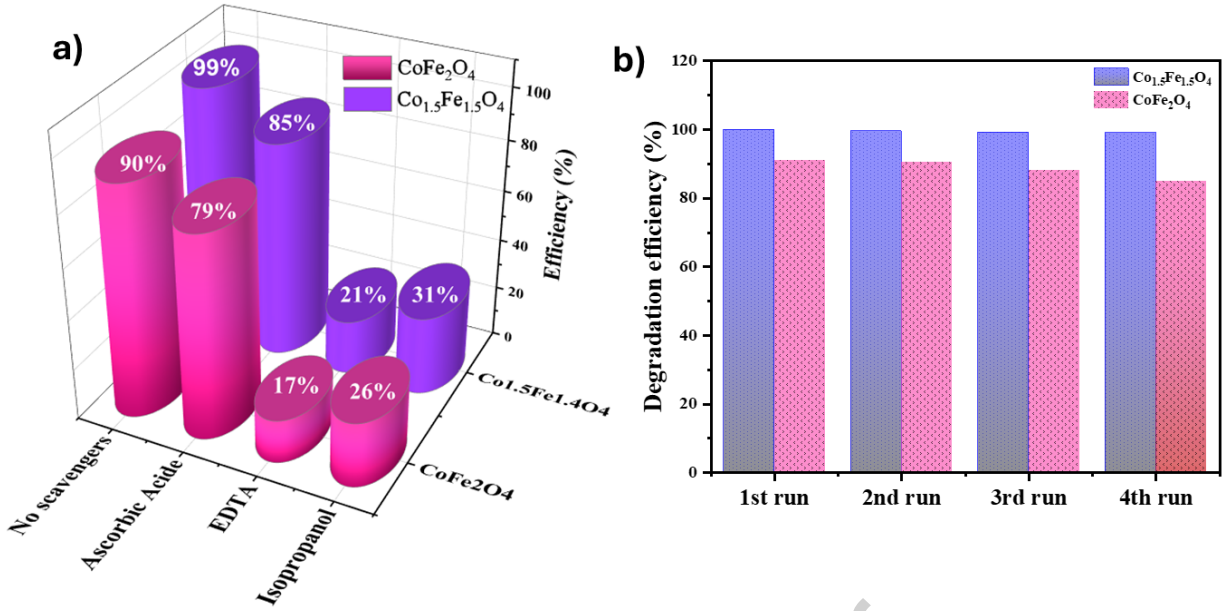


**Fig. 9.** (a) Radical trapping tests and (b) Recycling test using $CoFe_2O_4$ and $Co_{1.5}Fe_{1.5}O_4$ (measurements after 180 minutes)

Recyclability is an important factor which determines the suitability of the photocatalyst for practical use in real applications. To investigate this critical aspect, the recyclability of the two photocatalyst was evaluated under optimized conditions for the photodegradation of Rhodamine B. After each test, the catalyst $Co_xFe_{3-x}O_4$ was recovered using a magnet [20], then washed with distilled water and dried at 80°C to ensure its availability for the next cycle. These results showed that the $Co_xFe_{3-x}O_4$ photocatalyst can be easily recycled and reused in the water solution, highlighting the potential for practical applications. As shown in Fig. 9.b, $Co_{1.5}Fe_{1.5}O_4$ repeatedly maintains a high degradation efficiency near to 100% across all runs, indicating excellent stability and recyclability. Meanwhile, $CoFe_2O_4$ shows a slight decrease in efficiency during the same period, indicating a gradual loss of activity close to 10%. This reduction in photocatalytic activity may be attributed to the deactivation of active sites on the surfaces of recycle $CoFe_2O_4$ photocatalysts [58,59].

3.6.4. The total organic carbon (TOC) analyzes:

Fig. 10 presents the TOC removal rate as well as the degradation efficiency (measured by UV-visible) using $CoFe_2O_4$ and $Co_{1.5}Fe_{1.5}O_4$ after 180 min of irradiation under simulated sunlight. The TOC value of initial solution was found to be 6.8 ppm, corresponding to 10 ppm of RhB, after 180 minutes of irradiation in the presence of $CoFe_2O_4$, the TOC level drops to 1.1 ppm, corresponding to approximately 83% removal of organic carbon. For $Co_{1.5}Fe_{1.5}O_4$, TOC value after the same time of irradiation is 0.3 ppm which corresponds to 97% of reduction. The results clearly confirm that the organic carbon from the RhB molecules has been efficiently degraded, demonstrating true photodegradation and not simply decolorization.

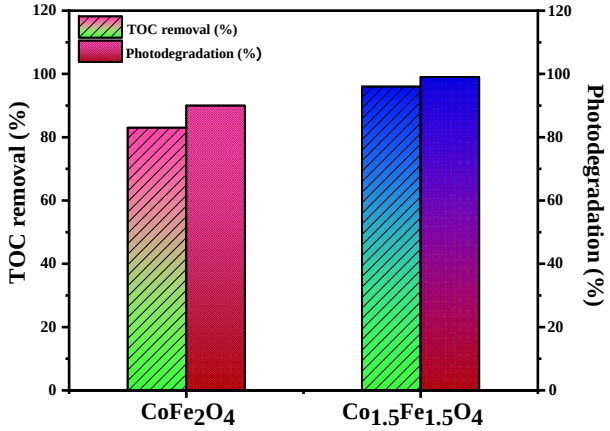


**Fig. 10:** TOC removal and photodegradation rate of RhB using $CoFe_2O_4$ and $Co_{1.5}Fe_{1.5}O_4$.

3.6.5. Mott-Schottky measurement

For the photocatalytic mechanism, the position of the valence band (VB) and the conduction band (CB) of the $Co_xFe_{3-x}O_4$ ferrite are important data that have been evaluated from the Mott-Schottky (MS) plots measured at 500 Hz (Fig. 11.a). The Mott-Schottky Equation (8), which relates the applied potential to the carrier density, is expressed as follows [60]:

$$\frac{1}{C^2} = \frac{2}{\varepsilon\varepsilon_0 A^2 e N_D}\left(V - V_{Fb} - \frac{k_B T}{e}\right) \qquad (8)$$

Where C is the interfacial capacitance, A is the area of catalyst, $N_D$ indicates the number of donors, V represents the applied voltage, $k_B$ is the Boltzmann constant, T is the absolute temperature and e the elementary charge. Hence, by plotting $\frac{1}{c^2}$ versus voltage (V), a curve is obtained from which the flat band potential $V_{fb}$ can be determined by extrapolating the linear part of the curve and its intersection with the voltage axis. The linear variation of $\frac{1}{c^2}$ with applied potential and a positive slope are observed in the MS plots (Fig. 11.a) which confirm that $Co_xFe_{3-x}O_4$ photocatalyst are n-type semiconductors [61–64]. The $V_{fb}$ values for $CoFe_2O_4$ and $Co_{1.5}Fe_{1.5}O_4$ were found to be -0.28 V and -0.17 V vs. Ag/AgCl, respectively. Moreover, the normal hydrogen electrode (NHE) potential of the $Co_xFe_{3-x}O_4$ nanoparticles can be calculated by the following Equation (9) [65]:

$$E_{Ag/Agcl} = E_{NHE} - 0.197 \qquad (9)$$

where $E_{Ag/AgCl}$ is the potential measured in relation with the Ag/AgCl reference electrode and $E_{NHE}$ is the potential expressed in the NHE scale. The $Co_xFe_{3-x}O_4$ photocatalyst band-structure can be determined by applying the equations below Equations (10)-(11)[66–68]:

$$E_{CB} = V_{fb} - 0.2V \qquad (10)$$

$$E_g = E_{VB} - E_{CB} \qquad (11)$$

where $E_{CB}$ and $E_{VB}$ is the conduction and the valence band potential respectively, $V_{fb}$ is the flat band potential and $E_g$ is the band gap energy.

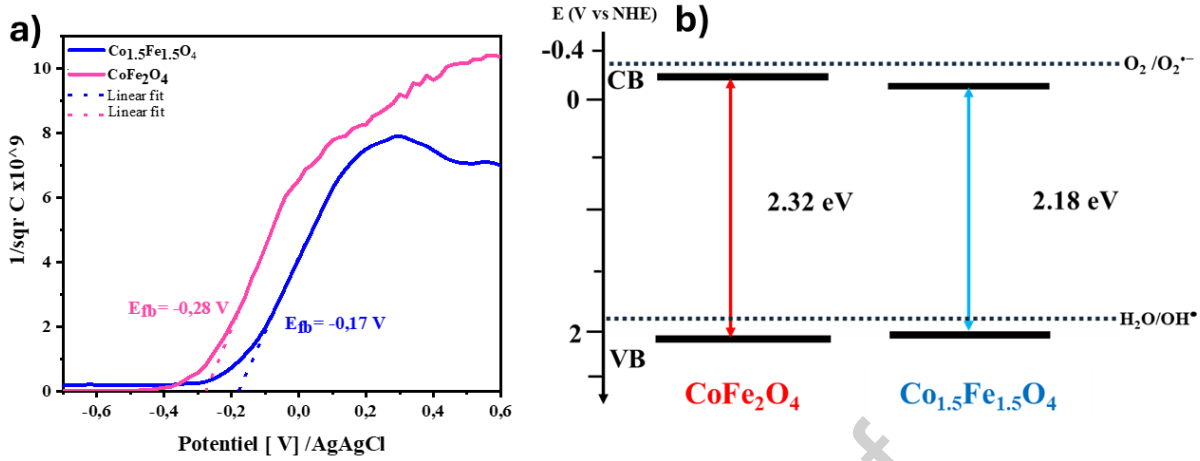


**Fig. 11.** (a) Mott-Schottky graphs and (b) representation of the VB and CB potential in the NHE scale for $CoFe_2O_4$ and $Co_{1.5}Fe_{1.5}O_4$

The CB potentials of the $CoFe_2O_4$ and $Co_{1.5}Fe_{1.5}O_4$ nanoparticles were found to be -0.28 V and -0.17 V.vs NHE, respectively. To obtain VB potential, the band gap energy $E_g$ previously determined by the DRS technique is added to the conduction band potential $E_{CB}$ according to equation (11). From the CB potentials and band gap values, the VB potentials for $CoFe_2O_4$ and $Co_{1.5}Fe_{1.5}O_4$ nanoparticles were calculated to be 2.04 V and 2.01V vs. NHE, respectively. The valence and conduction band positions for both materials, $CoFe_2O_4$ and $Co_{1.5}Fe_{1.5}O_4$, are presented in Fig. 9.b. The energy diagram allows us to set the redox potential of the active radicals around the VB and CB potentials. This representation shows that the superoxide redox potential is more negative than the CB potential indicating the lower contribution of the $O2^{\bullet-}$ radicals in the photo-degradation processes. However, the VB potential is more positive than the hydroxyl redox potential, which explain the main role of the hydroxyl radicals in the RhB degradation, the results of the previous scavengers' tests are corroborated by the position of the redox couple's potential of the reactive species.

### 3.6.6. General discussion

The photocatalytic results showed that the complete degradation of Rhodamine B was achieved for the two ferrite compositions ($CoFe_2O_4$ and $Co_{1.5}Fe_{1.5}O_4$), indicating comparable photocatalytic behavior. This similarity can be attributed to a close average grain sizes shown by MET measurements, and in the two cases the grains have a nano-octahedral shape. The BET measurements revealed a surface area of 102 $m^2/g$ for $CoFe_2O_4$ is, and 106 $m^2/g$ for $Co_{1.5}Fe_{1.5}O_4$. This small difference in surface area (< 4%) is not enough to impact on their photocatalytic activity. As the photocatalysis is a surface process, this high value of specific surface area indicates that the two materials provide

a nearly equivalent number of active sites for adsorption on surface and degradation of Rhodamine B [69]. The notable difference that exists in the behavior of the ferrites is at the level of the complete degradation time: $Co_{1.5}Fe_{1.5}O_4$ degrades faster RhB (180 minutes) than $CoFe_2O_4$ (240 minutes). This performance improvement for x = 1.5 may be attributed to changes in its electronic structure due to the increase of cobalt content. In fact, there is a decrease in the band gap energy: from 2.32 eV (x= 1) to 2.18 eV (x=1.5), a narrower bandgap energy allows greater absorption of visible radiation, which leads to a higher photogenerated charge density [70]. In addition, fluorescence spectroscopy (FL) measurements reveal a higher FL peaks intensity in $CoFe_2O_4$ compared to those of $Co_{1.5}Fe_{1.5}O_4$, and it is known that the FL peak intensity is correlated with the recombination rate of photo-generated charge carriers (electrons and holes). In this case, more $e^-/h^+$ pair recombination occur in $CoFe_2O_4$ which reduces the quantity of active species for photocatalytic reactions and therefore reduces the degradation rate [71]. Furthermore, the photocurrent response analysis indicates that $Co_{1.5}Fe_{1.5}O_4$ exhibits a higher photocurrent response compared to $CoFe_2O_4$. This highest value suggests that more electrons and holes are photogenerated and transported in $Co_{1.5}Fe_{1.5}O_4$ leading to faster dye degradation [72]. Finally, electrochemical impedance spectroscopy (EIS) shows a lower charge transfer resistance for x=1.5 compared to x=1, that enhancing the charge carrier movement across the photocatalyst surface [73] and therefore facilitates the RhB degradation.

The trapping tests for reactive chemical species made it possible to highlight those which are involved in the degradation of rhodamine. These mainly concern hydroxyls radicals ($OH^\bullet$) and holes ($h^+$), with superoxide radicals ($O_2^{\bullet-}$) playing a more minor role. To complete the experimental part of the study, it is important to position the energy levels of the different parameters involved in the photocatalytic process. Fig. 10 shows the valence band (VB) and conduction band (CB) potential for the two compositions of ferrite. Following, the radical trapping tests, the potentials of the $O_2/O_2^{\bullet-}$ and $H_2O/OH^\bullet$ redox couples are also considered (-0.33 V and 1.99 V with reference to the normal hydrogen electrode (NHE), respectively) [74,75]. The position of the redox potential of the radical species with respect to the position of the VB and CB bands of $Co_xFe_{3-x}O_4$ allows us to identify the radical's species which can be active during the process. As illustrated in Fig. 12, the VB potential of the two samples is more positive than the potential of the $H_2O/OH^\bullet$ redox couple which means that, from a thermodynamic point of view, compounds have the ability to generate hydroxyl radicals ($OH^\bullet$) [76]. On the other hand, the CB potential of the $Co_xFe_{3-x}O_4$ catalyst is more positive to the potential of the $O_2^{\bullet-}/O_2$ redox couple, so generation of superoxide radicals ($O_2^{\bullet-}$) may not be favored [77]. These thermodynamic considerations are in agreement with the radical trapping tests, for which hydroxyl radicals ($OH^\bullet$) and holes ($h^+$) were identified as oxidizing species, playing the major role in the photodegradation of RhB.

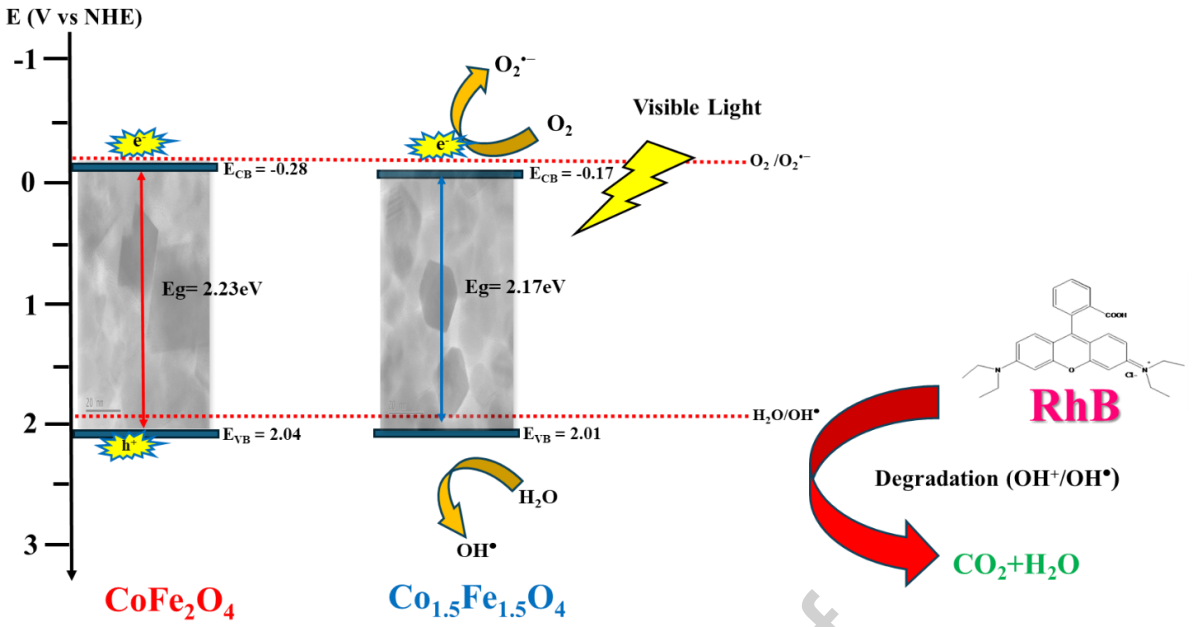


**Fig. 12.** The proposed mechanism for Photodegradation of RhB using $Co_xFe_{3-x}O_4$.

Consequently, the photodegradation of RhB in the presence of the $Co_xFe_{3-x}O_4$ semiconductor photocatalyst consists of an initial excitation of the semiconductor by the absorption of light energy, leading to the generation of electron-hole pairs according to Equation (12). The holes photogenerated in the valence band of the $Co_xFe_{3-x}O_4$ semiconductor react with water molecules present in the solution to form highly reactive hydroxyl radicals ($OH^{\bullet}$) Equation (13). The photo-generated electrons in the conduction band react with the oxygen dissolved in the solution to form reactive superoxide radicals ($O_2^{\bullet-}$), which, in our case, do not play a primary role Equation (14)

$$Co_xFe_{3-x}O_4 + hv \rightarrow Co_xFe_{3-x}O_4(e^-, h^+) \quad (12)$$

$$H_2O + h^+ \rightarrow OH^{\bullet} + H^+ \quad (13)$$

$$O_2 + e^- \rightarrow O_2^{\bullet-} \quad (14)$$

$$RhB + OH^{\bullet} \rightarrow CO_2 + H_2O + \text{intermediate compounds.} \quad (15)$$

$$RhB + O_2^{\bullet-} \rightarrow CO_2 + H_2O + \text{intermediate compounds.} \quad (16)$$

The hydroxyl radicals ($OH^{\bullet}$) generated during the photocatalytic process are the primary oxidizing agents responsible for the degradation of Rhodamine B. These reactive oxygen species (ROS) can effectively degrade dye molecules, through a series of oxidation reactions [78]. As shown by the TOC analyses, the oxidation reactions led to an advanced stage of mineralization, giving rise to carbon dioxide and water Equation (15) [79]. Even if the role of superoxide radicals ($O_2^{\bullet-}$) is less important, they still participate in RhB degradation according to Equation (16).

These experimental results must be compared to those in the literature, some of which are mentioned in table 4. For the comparison, several parameters were taken into account. It is often

mentioned that the synthesis method has an influence on the cationic repartition in the ferrite structure (tetrahedral/octahedral sites) leading to a n or p type semiconductor [80]. The morphology and the size of the particles play a role at the level of the reactivity of the particles, the small ones being more reactive. The faceted particles exhibited different crystallographic plans: (100) for a cube and (111) for an octahedron, the cations underlying these planes can be different and change the reactivity of the faces [19]. The other parameters concerning the conditions of the photocatalytic application are (pH, initial RhB concentration and mass of photocatalyst). In this work, $CoFe_2O_4$ was prepared by hydrothermal method showed a 100% RhB photodegradation (10 ppm) within 240 minutes, which exceeds various reported results in the literature (Table 4). Ferreira et al. [82] synthesized spherical $CoFe_2O_4$ nanoparticles with a grain size of 75 nm, achieving 90.9% photodegradation of Rhodamine B (RhB) at a concentration of 5 ppm over 240 minutes using 0.1 g/L of catalyst. In comparison, Loan et al. produced spherical $CoFe_2O_4$ particles with a smaller grain size of 20 nm, which resulted in 91% degradation after 270 minutes with a higher catalyst concentration of 1 g/L for RhB at 10 ppm [81], and using our Response Surface Methodology (RSM) model, we predicted the degradation efficiency under similar conditions and achieved 98.7% after 240 minutes, indicating superior performance. The increased activity of our cobalt ferrite catalyst is attributed to the smaller particle size (9 nm) and the uniform nano-octahedral morphology, which increases the surface area and improves the charge separation, critical parameters for photocatalytic efficiency.

In a second step, doped cobalt ferrites are compared to our synthesized $CoFe_2O_4$ which remains competitive. For instance, Abdo et al. [82] synthesized $Co_{0.5}Cu_{0.5}Fe_2O_4$ using the combustion method, obtaining a spherical morphology but achieving only 22% RhB photodegradation after 270 minutes using 5 ppm RhB and 1 g/L of catalyst. $Co_{0.6}Mg_{0.4}Fe_2O_4$ prepared by the combustion method achieved 99% RhB removal in 250 minutes [40]. The $Co_xFe_{3-x}O_4$ ferrite for x= 1 shows competitive results.

In this work, another composition x=1.5, never reported in the literature in the field of photocatalyst, was tested and showed 100% RhB degradation in only 180 minutes. This remarkable result is likely due to changes in its electronic structure, resulting in a smaller bandgap and enhanced carrier mobility, leading to faster degradation. These results show that $Co_{1.5}Fe_{1.5}O_4$ is a promising and highly efficient photocatalyst, exceeding both undoped and doped $CoFe_2O_4$ or composite variants.

**Table 4**: Summary of the photocatalytic activities of cobalt ferrite in the Literature.

| Photocatalyst | Synthesis method | Morphology | Grain size | [RhB] (ppm) | Catalyst dose (g/L) | Reaction time (min) | Removal efficiency (%) | Ref |
|---|---|---|---|---|---|---|---|---|
| $CoFe_2O_4$ | Co-precipitation | Spherical-shaped | 58 | 5 | 0.5 | 180 | 34 | [83] |
| $CoFe_2O_4$ | sol-gel | Nano-cubic | 38 | 5 | 0.6 | 120 | 28 | [84] |

| | | | | | | | | |
|---|---|---|---|---|---|---|---|---|
| $CoFe_2O_4$ | combustion method | Spherical | 20 | 10 | 1 | 270 | 91 | [81] |
| $CoFe_2O_4$ | microwave-assisted combustion | Irregular shaped | 46 | 6 | 0.31 | 300 | 100 | [40] |
| $CoFe_2O_4$ | Co-precipitation | Irregular shaped | - | 5 | 0.1 | 90 | 37 | [85] |
| $CoFe_2O_4$ | Co-precipitation | Quasi-spherical | - | 5 | 0.6 | 180 | 28 | [86] |
| $CoFe_2O_4$ | Co-precipitation | Spherical shape | 75 | 5 | 0.1 | 240 | 90.9 | [87] |
| $CoFe_2O_4$ | Hydrothermal | Nano-octahedral | 9 | 10 | 0.95 | 240 | 100 | **Present Work** |
| $Co_{0.6}Mg_{0.4}Fe_2O_4$ | Combustion method | Irregular shaped | 39 | 6 | 0.31 | 250 | 100 | [40] |
| $Ni_{0.1}Co_{0.9}Fe_2O_4$ | Co-precipitation | Irregular shaped | - | 5 | 0.1 | 90 | 83 | [85] |
| $Co_{0.5}Cu_{0.5}Fe_2O_4$ | Combustion method | spherical shape | - | 5 | 1 | 270 | 22 | [82] |
| $Co_{1.5}Fe_{1.5}O_4$ | Hydrothermal | Nano-octahedral | 8 | 10 | 0.95 | 180 | 100 | **Present Work** |

## 4. Conclusions

$Co_xFe_{3-x}O_4$ cobalt ferrites with two compositions (x=1 and x=1.5) were synthesized using a hydrothermal method for application in photocatalysis. From the structural point of view, the powders obtained show monocrystalline grains of nanometric size (8-9 nm) and octahedral shape, and they exhibited a high specific surface area (over 100 $m^2.g^{-1}$), which makes them potentially powders highly reactive. The combined optical and electrochemical measurements determined the semiconductor type (n for both compositions) and their gap energy 2.32eV and 2.18 eV for x=1 and x=1.5 respectively, showing that they are sensitive to visible radiation. The photocatalysis tests were carried out on a Rhodamine B solution, and their optimization was performed on the $CoFe_2O_4$ sample by considering three experimental parameters of the test (concentration and pH of the initial polluted solution, mass of the catalyst). The use of the response surface methodology (RSM) method enabled the determination of conditions to achieve complete degradation, these were then validated experimentally. The chemical species trapping tests and the study of the potentials of BV, BC and redox couples revealed that hydroxyl radicals ($OH^{\bullet}$) were the main actors in the degradation process of RhB, with superoxide radicals ($O_2^{\bullet-}$) playing a less important role. Finally, the composition x=1.5, never tested in photocatalysis, shows that complete degradation is obtained more quickly than with x=1 and that the efficiency value is preserved after 4 cycles. Thanks to the TOC results, we can see that the degradation has allowed an advanced mineralization. These results show that for the composition x= 1, the efficiency is in the same range that reported in the literature. Moreover, the composition x = 1.5 presents a better efficiency than for x = 1 but also than the doped ferrites or the

composites reported in the literature. To further improve performance, studies are currently in progress on metallic cation -doped cobalt ferrite.

**Acknowledgements:**

The authors gratefully acknowledge the Regional Council of Provence-AlpesCote d'Azur, Departmental Council of Var (CD83), the urban community of Toulon Provence Mediterranean and University of Toulon for their financial supports in the framework of the "NanoCat", "Disolar" and "NSPEC" projects. Conflicts of Interest: The author declares that he has no known competing financial interest or personal relationships that could have appeared to influence the work reported in this paper.

**References**

[1] V.S. Kirankumar, S. Sumathi, A review on photodegradation of organic pollutants using spinel oxide, Mater. Today Chem.18 (2020) 100355. https://doi.org/10.1016/j.mtchem.2020.100355.

[2] L. Lin, H. Yang, X. Xu, Effects of Water Pollution on Human Health and Disease Heterogeneity: A Review, Front. Environ. Sci. 10 (2022). https://doi.org/10.3389/fenvs.2022.880246.

[3] A.L. Boreen, W.A. Arnold, K. McNeill, Photodegradation of pharmaceuticals in the aquatic environment: A review, Aquat. Sci. 65 (2003) 320–341. https://doi.org/10.1007/s00027-003-0672-7.

[4] J.A. Garrido-Cardenas, B. Esteban-García, A. Agüera, J.A. Sánchez-Pérez, F. Manzano-Agugliaro, Wastewater Treatment by Advanced Oxidation Process and Their Worldwide Research Trends, Int J Environ Res Public Health 17 (2020) 170. https://doi.org/10.3390/ijerph17010170.

[5] Y. Deng, R. Zhao, Advanced Oxidation Processes (AOPs) in Wastewater Treatment, Curr Pollution Rep 1 (2015) 167–176. https://doi.org/10.1007/s40726-015-0015-z.

[6] K.M. Lee, C.W. Lai, K.S. Ngai, J.C. Juan, Recent developments of zinc oxide based photocatalyst in water treatment technology: A review, Water Research 88 (2016) 428–448. https://doi.org/10.1016/j.watres.2015.09.045.

[7] S.-Y. Lee, S.-J. Park, TiO2 photocatalyst for water treatment applications, Journal of Industrial and Engineering Chemistry 19 (2013) 1761–1769. https://doi.org/10.1016/j.jiec.2013.07.012.

[8] Sonia, H. Kumari, Suman, S. Chahal, S. Devi, S. Kumar, S. Kumar, P. Kumar, A. Kumar, Spinel ferrites/metal oxide nanocomposites for waste water treatment, Appl. Phys. A 129 (2023) 91. https://doi.org/10.1007/s00339-022-06288-0.

[9] X. Xie, B. Wang, Y. Wang, C. Ni, X. Sun, W. Du, Spinel structured MFe2O4 (M = Fe, Co, Ni, Mn, Zn) and their composites for microwave absorption: A review, Chemical Engineering Journal 428 (2022) 131160. https://doi.org/10.1016/j.cej.2021.131160.

[10] A. Soufi, H. Hajjaoui, R. Elmoubarki, M. Abdennouri, S. Qourzal, N. Barka, Spinel ferrites nanoparticles: Synthesis methods and application in heterogeneous Fenton oxidation of organic pollutants – A review, Applied Surface Science Advances 6 (2021) 100145. https://doi.org/10.1016/j.apsadv.2021.100145.

[11] F. Wang, L. Zhu, Q. Wei, Y. Wang, Research on the effects of hydrothermal synthesis conditions on the crystal habit of MIL-121, Royal Society Open Science 7 (2020) 201212. https://doi.org/10.1098/rsos.201212.

[12] H. Lee, S.H. Park, Y.-K. Park, B.H. Kim, S.-J. Kim, S.-C. Jung, Rapid destruction of the rhodamine B using TiO2photocatalyst in the liquid phase plasma, Chemistry Central Journal 7 (2013) 156. https://doi.org/10.1186/1752-153X-7-156.

[13] A.A. Al-Kahtani, Photocatalytic Degradation of Rhodamine B Dye in Wastewater Using Gelatin/CuS/PVA Nanocomposites under Solar Light Irradiation, Journal of Biomaterials and Nanobiotechnology 8 (2016) 66–82. https://doi.org/10.4236/jbnb.2017.81005.

[14] R. Gao, W. Lin, Y. Zhang, X. Mai, J. Chen, H. Lin, Photocatalytic degradation of RhB in wastewater by zinc ion-doped Bi5O7I, New J. Chem. 48 (2024) 12306–12314. https://doi.org/10.1039/D3NJ05849B.

[15] Meenu, M. Vashishtha, S.O. Meena, Determination of optimized process variables using RSM-BBD for the production of biochar derived from mustard straws, Biomass Conv. Bioref. (2023). https://doi.org/10.1007/s13399-023-04981-5.

[16] J. Hu, X. Bian, Y. Xia, M. Weng, W. Zhou, Q. Dai, Application of response surface methodology in electrochemical degradation of amoxicillin with Cu-PbO2 electrode: Optimization and mechanism, Separation and Purification Technology 250 (2020) 117109. https://doi.org/10.1016/j.seppur.2020.117109.

[17] T.V. Tran, H.-T.T. Nguyen, H.H. Dang, D.T.C. Nguyen, D.H. Nguyen, T.V. Pham, L.V. Tan, Central composite design for optimizing the organic dyes remediation utilizing novel graphene oxide@CoFe2O4 nanocomposite, Surfaces and Interfaces 21 (2020) 100687. https://doi.org/10.1016/j.surfin.2020.100687.

[18] L. Van Tan, N. Thi Hong Tham, V. Thuan Tran, D. Thi To Uyen, P. Van Thinh, Statistical analysis of expanded graphite-decorated cobalt ferrite as adsorbent for removal of Congo Red dye using response surface methodology, Materials Today: Proceedings 38 (2021) 2737–2744. https://doi.org/10.1016/j.matpr.2020.08.568.

[19] A.L. Lopes-Moriyama, V. Madigou, C.P.D. Souza, C. Leroux, Controlled synthesis of CoFe2O4 nano-octahedra, Powder Technology 256 (2014) 482–489. https://doi.org/10.1016/j.powtec.2014.01.080.

[20] L. Ajroudi, N. Mliki, L. Bessais, V. Madigou, S. Villain, Ch. Leroux, Magnetic, electric and thermal properties of cobalt ferrite nanoparticles, Materials Research Bulletin 59 (2014) 49–58. https://doi.org/10.1016/j.materresbull.2014.06.029.

[21] Z. Erbas, M. Soylak, Determination of Rhodamine B by UV–Vis spectrophotometry in cosmetics after microextraction by using heat-induced homogeneous liquid–liquid extraction method, J IRAN CHEM SOC 19 (2022) 3935–3942. https://doi.org/10.1007/s13738-022-02579-8.

[22] H. Wang, M. Yu, C.K. Lin, J. Lin, Core–shell structured SiO2@YVO4:Dy3+/Sm3+ phosphor particles: Sol–gel preparation and characterization, Journal of Colloid and Interface Science 300 (2006) 176–182. https://doi.org/10.1016/j.jcis.2006.03.052.

[23] S. Murakami, M. Herren, D. Rau, M. Morita, Photoluminescence and decay profiles of undoped and Fe3+, Eu3+-doped PLZT ceramics at low temperatures down to 10 K, Inorganica Chimica Acta 300–302 (2000) 1014–1021. https://doi.org/10.1016/S0020-1693(00)00008-6.

[24] M. Zubair, H.A. Aziz, I. Ihsanullah, M.A. Ahmad, M.A. Al-Harthi, Enhanced removal of Eriochrome Black T from water using biochar/layered double hydroxide/chitosan hybrid composite: Performance evaluation and optimization using BBD-RSM approach, Environmental Research 209 (2022) 112861. https://doi.org/10.1016/j.envres.2022.112861.

[25] S. Merabet, A. Bouzaza, M. Bouhelassa, D. Wolbert, Modélisation et optimisation de la photodégradation du 4-méthylphénol dans un réacteur à recirculation en présence d'UV/ZnO, rseau 22 (2009) 565–573. https://doi.org/10.7202/038331ar.

[26] D.R. Pinheiro, R. de F. Neves, S.P.A. Paz, A sequential Box-Behnken Design (BBD) and Response Surface Methodology (RSM) to optimize SAPO-34 synthesis from kaolin waste, Microporous and Mesoporous Materials 323 (2021) 111250. https://doi.org/10.1016/j.micromeso.2021.111250.

[27] R. Behura, R. Sakthivel, N. Das, Synthesis of cobalt ferrite nanoparticles from waste iron ore tailings and spent lithium ion batteries for photo/sono-catalytic degradation of Congo red, Powder Technology 386 (2021) 519–527. https://doi.org/10.1016/j.powtec.2021.03.066.

[28] S.B. Waje, M. Hashim, W.D.W. Yusoff, Z. Abbas, X-ray diffraction studies on crystallite size evolution of CoFe2O4 nanoparticles prepared using mechanical alloying and sintering, Applied Surface Science 256 (2010) 3122–3127. https://doi.org/10.1016/j.apsusc.2009.11.084.

[29] V. Calero-DiazdelCastillo, C. Rinaldi, Synthesis and magnetic characterization of cobalt-substituted ferrite (CoxFe3−xO4) nanoparticles, Journal of Magnetism and Magnetic Materials 314 (2007) 60–67. https://doi.org/10.1016/j.jmmm.2006.12.030.

[30] I. Ibrahim, A. Kaltzoglou, C. Athanasekou, F. Katsaros, E. Devlin, A.G. Kontos, N. Ioannidis, M. Perraki, P. Tsakiridis, L. Sygellou, M. Antoniadou, P. Falaras, Magnetically separable TiO2/CoFe2O4/Ag nanocomposites for the photocatalytic reduction of hexavalent chromium pollutant under UV and artificial solar light, Chemical Engineering Journal 381 (2020) 122730. https://doi.org/10.1016/j.cej.2019.122730.

[31] Y. Ortega López, H. Medina Vázquez, J. Salinas Gutiérrez, V. Guzmán Velderrain, A. López Ortiz, V. Collins Martínez, Synthesis Method Effect of CoFe2O4 on Its Photocatalytic Properties for H2 Production from Water and Visible Light, Journal of Nanomaterials 2015 (2015) 985872. https://doi.org/10.1155/2015/985872.

[32] M. Thommes, K. Kaneko, A.V. Neimark, J.P. Olivier, F. Rodriguez-Reinoso, J. Rouquerol, K.S.W. Sing, Physisorption of gases, with special reference to the evaluation of surface area and pore size distribution (IUPAC Technical Report), Pure and Applied Chemistry 87 (2015) 1051–1069. https://doi.org/10.1515/pac-2014-1117.

[33] A. Nasiri, M. Malakootian, M.R. Heidari, S.N. Asadzadeh, CoFe2O4@Methylcelloluse as a New Magnetic Nano Biocomposite for Sonocatalytic Degradation of Reactive Blue 19, J Polym Environ 29 (2021) 2660–2675. https://doi.org/10.1007/s10924-021-02074-w.

[34] R. Tabit, O. Amadine, Y. Essamlali, K. Dânoun, A. Rhihil, M. Zahouily, Magnetic $CoFe_2O_4$ nanoparticles supported on graphene oxide ($CoFe_2O_4$/GO) with high catalytic activity for peroxymonosulfate activation and degradation of rhodamine B, RSC Adv. 8 (2018) 1351–1360. https://doi.org/10.1039/C7RA09949E.

[35] S. Omidi, A.M. Davarpanah, A.R. Abbasian, Enhancement of specific surface area of CoFe2O4 powders synthesized by KCl-assisted solution combustion: effect of KCl content and initial pH, Iranian Journal of Physics Research 22 (2022) 353–371. https://doi.org/10.47176/ijpr.22.2.61266.

[36] M. Safari, J. Mazloom, Electrochemical performance of spindle-like Fe2Co-MOF and derived magnetic yolk-shell CoFe2O4 microspheres for supercapacitor applications, J Solid State Electrochem 25 (2021) 2189–2200. https://doi.org/10.1007/s10008-021-04989-9.

[37] S. Landi, I.R. Segundo, C. Afonso, O. Lima, M.F.M. Costa, E. Freitas, J. Carneiro, Evaluation of band gap energy of TiO2 precipitated from titanium sulphate, Physica B: Condensed Matter 639 (2022) 414008. https://doi.org/10.1016/j.physb.2022.414008.

[38] P. Makuła, M. Pacia, W. Macyk, How To Correctly Determine the Band Gap Energy of Modified Semiconductor Photocatalysts Based on UV–Vis Spectra, J. Phys. Chem. Lett. 9 (2018) 6814–6817. https://doi.org/10.1021/acs.jpclett.8b02892.

[39] P. Laokul, S. Arthan, S. Maensiri, E. Swatsitang, Magnetic and Optical Properties of CoFe2O4 Nanoparticles Synthesized by Reverse Micelle Microemulsion Method, J Supercond Nov Magn 28 (2015) 2483–2489. https://doi.org/10.1007/s10948-015-3068-8.

[40] M. Sundararajan, L. John Kennedy, P. Nithya, J. Judith Vijaya, M. Bououdina, Visible light driven photocatalytic degradation of rhodamine B using Mg doped cobalt ferrite spinel nanoparticles synthesized by microwave combustion method, Journal of Physics and Chemistry of Solids 108 (2017) 61–75. https://doi.org/10.1016/j.jpcs.2017.04.002.

[41] Z. Zhou, Y. Zhang, Z. Wang, W. Wei, W. Tang, J. Shi, R. Xiong, Electronic structure studies of the spinel CoFe2O4 by X-ray photoelectron spectroscopy, Applied Surface Science 254 (2008) 6972–6975. https://doi.org/10.1016/j.apsusc.2008.05.067.

[42] A. Azouaoui, M. El Haoua, S. Salmi, A. El Grini, N. Benzakour, A. Hourmatallah, K. Bouslykhane, Structural and Magnetic Properties of Cd–Co Ferrites: Density Functional Theory Calculations and High-Temperature Series Expansions, J Supercond Nov Magn 33 (2020) 1831–1838. https://doi.org/10.1007/s10948-020-05429-x.

[43] A. El Aouni, M. El Ouardi, M. Arab, M. Saadi, H. Haspel, Z. Kónya, A. Ben Ali, A. Jada, A. BaQais, H. Ait Ahsaine, Design of Bismuth Tungstate Bi2WO6 Photocatalyst for Enhanced and Environmentally Friendly Organic Pollutant Degradation, Materials 17 (2024) 1029. https://doi.org/10.3390/ma17051029.

[44] L. Sun, Y. Wang, L. He, J. Guo, Q. Deng, X. Zhao, Y. Yan, K. Qi, Effect of cobalt doping on the photocatalytic performance of AgInS2 for organic pollutant degradation and hydrogen production, Journal of Alloys and Compounds 926 (2022) 166859. https://doi.org/10.1016/j.jallcom.2022.166859.

[45] M.A. Rahman, S. Bazargan, S. Srivastava, X. Wang, M. Abd-Ellah, J.P. Thomas, N.F. Heinig, D. Pradhan, K.T. Leung, Defect-rich decorated $TiO_2$ nanowires for super-efficient photoelectrochemical water splitting driven by visible light, Energy Environ. Sci. 8 (2015) 3363–3373. https://doi.org/10.1039/C5EE01615K.

[46] H. Feng, S. Feng, N. Tang, S. Zhang, X. Zhang, B. Liu, Fabrication of $TiO_2$ /$Fe_2O_3$ /CdS systems: effects of $Fe_2O_3$ and CdS content on superior photocatalytic activity, RSC Adv. 11 (2021) 10300–10308. https://doi.org/10.1039/D1RA00195G.

[47] S.N.S. Jefri, A.H. Abdullah, E.N. Muhamad, Response surface methodology: photodegradation of methyl orange by CuO/ZnO under UV light irradiation, Asain J. Green Chem. (2018). https://doi.org/10.22034/ajgc.2018.135387.1078.

[48] I.P.A.F. Souza, L.H.S. Crespo, L. Spessato, S.A.R. Melo, A.F. Martins, A.L. Cazetta, V.C. Almeida, Optimization of thermal conditions of sol-gel method for synthesis of TiO2 using RSM and its influence on photodegradation of tartrazine yellow dye, Journal of Environmental Chemical Engineering 9 (2021) 104753. https://doi.org/10.1016/j.jece.2020.104753.

[49] B.-E. Channab, M. El Ouardi, S.E. Marrane, O.A. Layachi, A. El Idrissi, S. Farsad, D. Mazkad, A. BaQais, M. Lasri, H. Ait Ahsaine, Alginate@$ZnCO_2O_4$ for efficient peroxymonosulfate activation towards effective rhodamine B degradation: optimization using response surface methodology, RSC Adv. 13 (2023) 20150–20163. https://doi.org/10.1039/D3RA02865H.

[50] T. Shojaeimehr, F. Rahimpour, M.A. Khadivi, M. Sadeghi, A modeling study by response surface methodology (RSM) and artificial neural network (ANN) on Cu2+ adsorption optimization using light expended clay aggregate (LECA), Journal of Industrial and Engineering Chemistry 20 (2014) 870–880. https://doi.org/10.1016/j.jiec.2013.06.017.

[51] K.L. Routray, S. Saha, D. Behera, N. Tripathy, S.P. Ghosh, High dielectric constant, low loss and efficient visible photoluminescence properties of porous rose- flower shaped CoFe2O4 for photovoltaic application, Materials Letters 242 (2019) 62–65. https://doi.org/10.1016/j.matlet.2019.01.114.

[52] Y. Jia, Z. Zhou, Y. Wei, Z. Wu, H. Wang, J. Chen, Y. Zhang, Y. Liu, Enhanced photoluminescence of core–shell CoFe2O4/SiO2/Y2O3:Eu3+ composite by remanent magnetization, Smart Mater. Struct. 22 (2013) 125014. https://doi.org/10.1088/0964-1726/22/12/125014.

[53] M. Akhtar, I. Bibi, F. Majid, A. Ghafoor, S. Kamal, G. Fatima, Q. Raza, N. Alwadai, A. Nazir, M. Iqbal, Photoluminescence, structural, optical, ferroelectric and photo-catalytic properties of magnetically separable CdO/CoFe2O4 hetero-junction, Ceramics International (2024) S0272884224002888. https://doi.org/10.1016/j.ceramint.2024.01.272.

[54] M. Goswami, Enhancement of photocatalytic activity of synthesized Cobalt doped Zinc Oxide nanoparticles under visible light irradiation, Optical Materials 109 (2020) 110400. https://doi.org/10.1016/j.optmat.2020.110400.

[55] T. Liu, L. Wang, X. Lu, J. Fan, X. Cai, B. Gao, R. Miao, J. Wang, Y. Lv, Comparative study of the photocatalytic performance for the degradation of different dyes by ZnIn 2 S 4 : adsorption, active species, and pathways, RSC Advances 7 (2017) 12292–12300. https://doi.org/10.1039/C7RA00199A.

[56] H. Liang, X. Tai, Z. Du, Photocatalytic degradation of nonylphenol ethoxylate and its degradation mechanism, Journal of Molecular Liquids 302 (2020) 112567. https://doi.org/10.1016/j.molliq.2020.112567.

[57] P. Molaei, F. Rahimi-Moghadam, Porous g-C3N4 nanosheets through facile thermal polymerization of melamine in the air for photocatalyst application, J Mater Sci: Mater Electron 32 (2021) 19655–19666. https://doi.org/10.1007/s10854-021-06488-z.

[58] X. Bai, W. Song, X. Ling, G. Linlong, D. Hao, X. Zhang, Metal ion endogenous cycles of CoFe2O4-x induced boosted photocatalytic/PMS degradation toward polycyclic aromatic hydrocarbons, Nanoscale (2023) 10.1039.D3NR00727H. https://doi.org/10.1039/D3NR00727H.

[59] J. de O. Soares, W.E.C. Cavalcanti, M.A.M. Torres, S.B.C. Pergher, F.J.V.E. De Oliveira, T.P. Braga, Synthesis, Characterization and Photocatalytic Activity of CoFe2O4/Fe2O3 Dispersed in Mesoporous KIT-6, Nanomaterials 12 (2022) 3566. https://doi.org/10.3390/nano12203566.

[60] A. Adán-Más, T.M. Silva, L. Guerlou-Demourgues, M.F. Montemor, Application of the Mott-Schottky model to select potentials for EIS studies on electrodes for electrochemical charge storage, Electrochimica Acta 289 (2018) 47–55. https://doi.org/10.1016/j.electacta.2018.08.077.

[61] N. Labchir, A. Hannour, A.A. Hssi, D. Vincent, K. Abouabassi, A. Ihlal, M. Sajieddine, Synthesis and characterization of CoFe2O4 thin films for solar absorber application, Materials Science in Semiconductor Processing 111 (2020) 104992. https://doi.org/10.1016/j.mssp.2020.104992.

[62] R. Nasser, H. Zhou, H. Elhouichet, S. Melhi, Z. Li, J.-M. Song, NiFe2O4@NiCo2O4 hollow algae-like microspheres enabled by Mott-Schottky for electrochemical energy storage, Chemical Engineering Journal 489 (2024) 151554. https://doi.org/10.1016/j.cej.2024.151554.

[63] X. Zhang, J. Zhang, Z. Ma, L. Wang, K. Yu, Z. Wang, J. Wang, B. Zhao, Ag engineered NiFe-LDH/NiFe2O4 Mott-Schottky heterojunction electrocatalyst for highly efficient oxygen evolution and urea oxidation reactions, Journal of Colloid and Interface Science 665 (2024) 313–322. https://doi.org/10.1016/j.jcis.2024.03.124.

[64] N. Labchir, E. Amaterz, A. Hannour, A. Ait hssi, D. Vincent, A. Ihlal, M. Sajieddine, Highly efficient nanostructured CoFe2O4 thin film electrodes for electrochemical degradation of rhodamine B, Water Environment Research 92 (2020) 759–765. https://doi.org/10.1002/wer.1272.

[65] C. Feng, Z. Lu, Y. Zhang, Q. Liang, M. Zhou, X. Li, C. Yao, Z. Li, S. Xu, A magnetically recyclable dual Z-scheme GCNQDs-CoTiO3/CoFe2O4 composite photocatalyst for efficient photocatalytic degradation of oxytetracycline, Chemical Engineering Journal 435 (2022) 134833. https://doi.org/10.1016/j.cej.2022.134833.

[66] M. El Ouardi, O. Ait Layachi, E. Amaterz, A. El Idrissi, A. Taoufyq, B. Bakiz, A. Benlhachemi, M. Arab, A. BaQais, H. Ait Ahsaine, Photo-electrochemical degradation of rhodamine B using electrodeposited Mn3(PO4)2.3H2O thin films, Journal of Photochemistry and Photobiology A: Chemistry 444 (2023) 115011. https://doi.org/10.1016/j.jphotochem.2023.115011.

[67] Y. Matsumoto, Energy Positions of Oxide Semiconductors and Photocatalysis with Iron Complex Oxides, Journal of Solid State Chemistry 126 (1996) 227–234. https://doi.org/10.1006/jssc.1996.0333.

[68] T. Cai, Y. Liu, L. Wang, S. Zhang, Y. Zeng, J. Yuan, J. Ma, W. Dong, C. Liu, S. Luo, Silver phosphate-based Z-Scheme photocatalytic system with superior sunlight photocatalytic activities and anti-photocorrosion performance, Applied Catalysis B: Environmental 208 (2017) 1–13. https://doi.org/10.1016/j.apcatb.2017.02.065.

[69] C. Bantz, O. Koshkina, T. Lang, H.-J. Galla, C.J. Kirkpatrick, R.H. Stauber, M. Maskos, The surface properties of nanoparticles determine the agglomeration state and the size of the particles under

physiological conditions, Beilstein J Nanotechnol 5 (2014) 1774–1786. https://doi.org/10.3762/bjnano.5.188.

[70] S. Guan, Y. Cheng, L. Hao, H. Yoshida, C. Tarashima, T. Zhan, T. Itoi, T. Qiu, Y. Lu, Oxygen vacancies induced band gap narrowing for efficient visible-light response in carbon-doped TiO2, Sci Rep 13 (2023) 14105. https://doi.org/10.1038/s41598-023-39523-6.

[71] M. Pal, A. Kundu, R. Rakshit, K. Mandal, Ligand-Induced Evolution of Intrinsic Fluorescence and Catalytic Activity from Cobalt Ferrite Nanoparticles, ChemPhysChem 16 (2015) 1627–1634. https://doi.org/10.1002/cphc.201500005.

[72] X. Liu, Y. Qin, Y. Yan, P. Lv, The fabrication of CdS/CoFe2O4/rGO photocatalysts to improve the photocatalytic degradation performance under visible light, RSC Adv. 7 (2017) 40673–40681. https://doi.org/10.1039/C7RA07202C.

[73] R. Zhang, Y. Li, Q. Han, T. Zhang, Y. Liu, K. Zeng, C. Zhao, Investigation the High Photocatalytic Activity of Magnetically Separable Graphene Oxide Modified BiOBr Nanocomposites for Degradation of Organic Pollutants and Antibiotic, J Inorg Organomet Polym 30 (2020) 1703–1715. https://doi.org/10.1007/s10904-019-01333-7.

[74] F. Liu, D. Su, W. Liu, B. Liu, C. Liu, H. Wang, M. Wang, Polar solvent induced in-situ self-assembly and oxygen vacancies on Bi2MoO6 for enhanced photocatalytic degradation of tetracycline, Nano Res. 17 (2024) 4951–4960. https://doi.org/10.1007/s12274-024-6498-4.

[75] T. Bak, J. Nowotny, M. Rekas, C.C. Sorrell, Photo-electrochemical hydrogen generation from water using solar energy. Materials-related aspects, International Journal of Hydrogen Energy 27 (2002) 991–1022. https://doi.org/10.1016/S0360-3199(02)00022-8.

[76] D. Wang, L. Guo, Y. Zhen, L. Yue, G. Xue, F. Fu, AgBr quantum dots decorated mesoporous Bi2WO6 architectures with enhanced photocatalytic activities for methylene blue, J. Mater. Chem. A 2 (2014) 11716–11727. https://doi.org/10.1039/C4TA01444H.

[77] Y. Liu, Y. Lin, Z. Liu, J. Tang, L. Chen, X. Liu, Y. Tian, D. Fang, J. Wang, Self-generating CoFe2O4 as electric channel in Z-scheme CoO(111)/CoFe2O4/Fe2O3 photocatalyst for synchronous photocatalytic degradation and hydrogen production, Materials Science in Semiconductor Processing 140 (2022) 106382. https://doi.org/10.1016/j.mssp.2021.106382.

[78] H.D. Tran, D.Q. Nguyen, P.T. Do, U.N.P. Tran, Kinetics of photocatalytic degradation of organic compounds: a mini-review and new approach, RSC Adv. 13 (2023) 16915–16925. https://doi.org/10.1039/D3RA01970E.

[79] H. Zhang, M. Li, W. Wang, G. Zhang, Q. Tang, J. Cao, Designing 3D porous BiOI/Ti3C2 nanocomposite as a superior coating photocatalyst for photodegradation RhB and photoreduction Cr (VI), Separation and Purification Technology 272 (2021) 118911. https://doi.org/10.1016/j.seppur.2021.118911.

[80] S. Ammar, N. Jouini, F. Fiévet, O. Stephan, C. Marhic, M. Richard, F. Villain, Ch. Cartier dit Moulin, S. Brice, Ph. Sainctavit, Influence of the synthesis parameters on the cationic distribution of ZnFe2O4 nanoparticles obtained by forced hydrolysis in polyol medium, Journal of Non-Crystalline Solids 345–346 (2004) 658–662. https://doi.org/10.1016/j.jnoncrysol.2004.08.162.

[81] N.T. To Loan, N.T. Hien Lan, N.T. Thuy Hang, N. Quang Hai, D.T. Tu Anh, V. Thi Hau, L. Van Tan, T. Van Tran, CoFe2O4 Nanomaterials: Effect of Annealing Temperature on Characterization, Magnetic, Photocatalytic, and Photo-Fenton Properties, Processes 7 (2019) 885. https://doi.org/10.3390/pr7120885.

[82] M.A. Abdo, A.A. El-Daly, Sm-substituted copper-cobalt ferrite nanoparticles: Preparation and assessment of structural, magnetic and photocatalytic properties for wastewater treatment applications, Journal of Alloys and Compounds 883 (2021) 160796. https://doi.org/10.1016/j.jallcom.2021.160796.

[83] V. Mahdikhah, S. Saadatkia, S. Sheibani, A. Ataie, Outstanding photocatalytic activity of CoFe2O4 /rGO nanocomposite in degradation of organic dyes, Optical Materials 108 (2020) 110193. https://doi.org/10.1016/j.optmat.2020.110193.

[84] S. Dharani, L. Gnanasekaran, S. Arunachalam, A. Zielińska-Jure, H.S. Almoallim, M. Soto-Moscoso, Photodegrading rhodamine B dye with cobalt ferrite-graphitic carbon nitride (CoFe2O4/g-C3N4) composite, Environmental Research 258 (2024) 119484. https://doi.org/10.1016/j.envres.2024.119484.

[85] J. Revathi, M.J. Abel, V. Archana, T. Sumithra, R. Thiruneelakandan, J. Joseph prince, Synthesis and characterization of CoFe2O4 and Ni-doped CoFe2O4 nanoparticles by chemical Co-precipitation technique for photo-degradation of organic dyestuffs under direct sunlight, Physica B: Condensed Matter 587 (2020) 412136. https://doi.org/10.1016/j.physb.2020.412136.

[86] M. Stefan, C. Leostean, A. Popa, D. Toloman, I. Perhaita, A. Cadis, S. Macavei, O. Pana, Highly stable MWCNT-CoFe2O4 photocatalyst. EGA-FTIR coupling as efficient tool to illustrate the formation

mechanism, Journal of Alloys and Compounds 928 (2022) 167188. https://doi.org/10.1016/j.jallcom.2022.167188.

[87] M.C.M. Ferreira, F.R. Praxedes, M.A.L. Nobre, S. Lanfredi, Synthesis of spinel ferrites and application in the photodegradation of Rhodamine in water via pH control assistance, Optical Materials 133 (2022) 113043. https://doi.org/10.1016/j.optmat.2022.113043.

## Graphical abstract

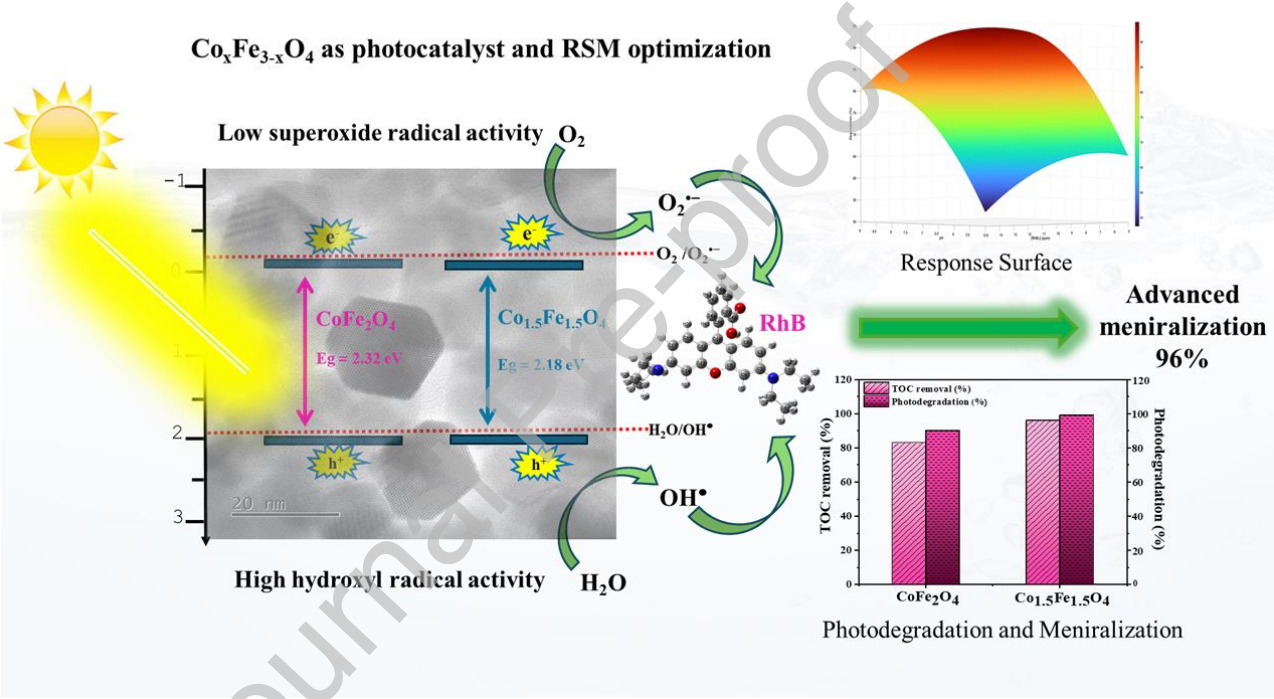


## Author statement

**Elaadssi Yassine**: Data curation; Formal analysis; Writing—original draft; Investigation

**Madjid Arab** and **Véronique Madigou**: Conceptualization; Project administration; Investigation, Writing—Review & Editing.

All authors have read and agreed to the published version of the manuscript.

**Declaration of interests**

☐ The authors declare that they have no known competing financial interests or personal relationships that could have appeared to influence the work reported in this paper.

☒ The authors declare the following financial interests/personal relationships which may be considered as potential competing interests:

Madjid ARAB reports was provided by University of Toulon. Madjid ARAB reports a relationship with University of Toulon that includes: employment, funding grants, and non-financial support. If there are other authors, they declare that they have no known competing financial interests or personal relationships that could have appeared to influence the work reported in this paper.